Characteristics of the ocean simulations in the Max Planck Institute Ocean Model (MPIOM) the ocean component of the MPI-Earth system model

J. H. Jungclaus,[1] N. Fischer,[1] H. Haak,[1] K. Lohmann,[1] J. Marotzke,[1] D. Matei,[1] U. Mikolajewicz,[1] D. Notz,[1] and J. S. von Storch[1]

Received 30 July 2012; revised 15 January 2013; accepted 20 February 2013; published 20 June 2013.

[1] MPI-ESM is a new version of the global Earth system model developed at the Max Planck Institute for Meteorology. This paper describes the ocean state and circulation as well as basic aspects of variability in simulations contributing to the fifth phase of the Coupled Model Intercomparison Project (CMIP5). The performance of the ocean/sea-ice model MPIOM, coupled to a new version of the atmosphere model ECHAM6 and modules for land surface and ocean biogeochemistry, is assessed for two model versions with different grid resolution in the ocean. The low-resolution configuration has a nominal resolution of 1.5°, whereas the higher resolution version features a quasiuniform, eddy-permitting global resolution of 0.4°. The paper focuses on important oceanic features, such as surface temperature and salinity, water mass distribution, large-scale circulation, and heat and freshwater transports. In general, these integral quantities are simulated well in comparison with observational estimates, and improvements in comparison with the predecessor system are documented; for example, for tropical variability and sea ice representation. Introducing an eddy-permitting grid configuration in the ocean leads to improvements, in particular, in the representation of interior water mass properties in the Atlantic and in the representation of important ocean currents, such as the Agulhas and Equatorial current systems. In general, however, there are more similarities than differences between the two grid configurations, and several shortcomings, known from earlier versions of the coupled model, prevail.

Citation: Jungclaus, J. H., N. Fischer, H. Haak, K. Lohmann, J. Marotzke, D. Matei, U. Mikolajewicz, D. Notz, and J. S. vonStorch (2013), Characteristics of the ocean simulations in MPIOM, the ocean component of the MPI-Earth system model, *J. Adv. Model. Earth Syst.*, *5*, 422–446, doi:10.1002/jame.20023.

1. Introduction

[2] The development of models used as tools for a better understanding of climate and environmental changes has evolved into two directions. On the one hand, increased computing power allows for much higher resolution in the major subcomponents ocean and atmosphere. On the other hand, models now include biogeochemical and, in part, chemical processes to study the complex interplay between air, water, and soil. Models including biogeochemical modules and an interactive carbon cycle are referred to as Earth system models (ESM). At the Max Planck Institute for Meteorology (MPI-M), this line of development can be seen in the evolution from the CMIP3 model, which included the European Center-Hamburg (ECHAM5) atmosphere model and the Max Planck Institute Ocean Model (MPIOM) [*Jungclaus et al.*, 2006] to the present MPI-ESM that is documented in this special issue of *Journal of Advances in Modeling Earth Systems*. First, the implementation of submodules for land surface processes and ocean biogeochemistry allowed for the simulation of an interactive carbon cycle, and the model participated in the Coupled Carbon Cycle Climate Model Intercomparison Project (C4MIP) [*Friedlingstein et al.*, 2006]. Using a coarse-resolution version of this model system, *Jungclaus et al.* [2010] demonstrated that it is possible to maintain a stable carbon cycle over thousands of years in a control experiment and carried out the first combined carbon cycle and climate simulations over the last millennium with a complex ESM. Toward CMIP5, further development work led to the development of the ECHAM6 atmosphere version, followed by the implementation of a dynamical vegetation model, technical improvements, and configurations with better representation of the stratosphere by enhanced vertical resolution.

[3] Along with several other manuscripts on various aspects of MPI-ESM in the special issue of *Journal of*

[1]Max Planck Institute for Meteorology, Bundesstrasse Hamburg, Germany.

1942-2466/13/10.1002/jame.20023

Advances in Modeling Earth Systems, this paper documents elements of the ocean circulation and oceanic properties. The ocean and sea-ice model MPIOM has remained basically unchanged from the previous coupled atmosphere ocean model ECHAM5/MPIOM [*Jungclaus et al*., 2006]. Also one of the grid configurations, the (now) low-resolution GR1.5, remained the same. The higher-resolution version of MPI-ESM features one of the highest ocean resolutions (0.4°) among all available CMIP5 models.

[4] We concentrate in this contribution on surface ocean and water mass properties and on integrated variables such as mass and heat transports. These are essential oceanic elements for the general performance of the coupled system. For our model configurations, we assess the effect of improving the horizontal ocean resolution from a noneddy-resolving nominal 1.5° grid to an eddy permitting 0.4°. Additional more general papers deal with the other subcomponents of MPI-ESM: ECHAM6, the atmospheric component of MPI-ESM, is documented by *Stevens et al*. [2013], the land-component Jena Scheme for Biosphere Atmosphere Coupling in Hamburg (JSBACH) is described by *Reick et al*. [2013], and the characteristics of the coupled system and basic climate change simulations are reported in M. Giorgetta et al. (Climate change from 1850 to 2100 in MPI-ESM simulations for the Coupled Model Intercomparison Project 5, manuscript submitted to *Journal of Advances in Modeling Earth Systems*, special issue of The Max Planck Institute for Meteorology Earth System Model).

[5] Because we here give a broad overview of the performance of the ocean component in the MPI-M CMIP5 simulations, several aspects cannot be described in detail and have been taken up by more dedicated studies as part of the MPI-ESM special issue: Arctic sea-ice evolution under historical and scenario boundary conditions are discussed by *Notz et al*. [2013], an evaluation of air-sea fluxes in A. Andersson et al. (Evaluation of MPI-ESM ocean surface fluxes, manuscript in preparation for *Journal of Advances in Modeling Earth Systems*, special issue of The Max Planck Institute for Meteorology Earth System Model, hereinafter referred to as Andersson, in preparation), and a study on land-surface fluxes and river runoff is provided by *Hagemann et al*. [2013]. The ocean biogeochemistry in the CMIP5 experiments as simulated by the Hamburg Ocean Carbon Cycle Model (HAMOCC5) is documented by *Ilyina et al*. [2013].

[6] The remainder of this paper is organized as follows. In section 2, MPIOM is described as part of the MPI-ESM. Section 3 describes the experimental configurations for the CMIP5 experiments under consideration, and section 4 explores the capability of MPIOM to represent the observed mean state of the ocean. Section 5 documents aspects of variability in the coupled system, and section 6 discusses in detail the issues of model-dependent representation of key features in the ocean. Section 7 concludes the manuscript with a summary.

2. Model

[7] The MPI-ESM consists of the general circulation models for the atmosphere ECHAM6 [*Stevens et al*., 2013] and for the ocean MPIOM [*Maier-Reimer*, 1997; *Marsland et al*., 2003; *Jungclaus et al*., 2006]. We describe here the model versions MPI-ESM-LR (LR, low resolution) and MPI-ESM-MR (MR, mixed resolution). ECHAM6 is run at T63 horizontal resolution (approximately 1.875° on a Gaussian grid) with 47 vertical levels in MPI-ESM-LR, and 95 levels in MPI-ESM-MR. Both setups resolve the troposphere and the stratosphere up to 0.01 hPa. Details of the ECHAM6 model physics and the development steps relative to the previous version, ECHAM5, can be found in *Stevens et al*. [2013]. The most important changes concern the shortwave radiative transfer, the representation of the land-surface including interactive vegetation, and the representation of the middle atmosphere as part of the default configuration (in CMIP3, ECHAM5 had 31 levels covering the atmosphere to 10 hPa). Changes in the shortwave physics have been combined with a revised surface albedo scheme and new representation of cloud optics. Over the ocean, ECHAM5 treated the surface albedo as constant, whereas ECHAM6 accounts for zenith angle [*Stevens et al*., 2013]. The albedo of sea ice and snow is calculated in ECHAM6, taking into account processes such as aging of snow and melt ponds on top of the sea ice [*Roeckner et al*., 2012].

[8] The carbon cycle comprises the ocean biogeochemistry module HAMOCC5 [*Ilyina et al*., 2013] and the land surface scheme JSBACH [*Reick et al*., 2013]. In MPI-ESM, the three-dimensional transport of carbon within the ocean and the atmosphere as well as the exchange between atmosphere and land biosphere are calculated at each time step while the exchange between ocean and atmosphere occurs at the coupling time step. In the particular CMIP5 simulations described here, atmospheric CO_2 concentrations are, however, not calculated interactively but prescribed, and fluxes between the compartments are diagnosed. Aspects of the carbon cycle in the MPI-ESM CMIP5 simulations are covered by Schneck et al. (The land contribution to natural CO_2 variability on time scales of centuries, manuscript submitted to *Journal of Advances in Modeling Earth Systems*, special issue of The Max Planck Institute for Meteorology Earth System Model) and *Ilyina et al*. [2013]. Another new feature in MPI-ESM is a module for dynamic vegetation [*Brovkin*, 2013].

[9] Ocean and atmosphere are coupled daily without flux adjustments using the Ocean Atmosphere Sea Ice Soil (OASIS3) coupler [*Valcke et al*., 2003]. Increasing the coupling frequency was not possible in this version of the model due to technical limitations in the hydrological discharge model. In the meantime, this issue has been solved and forthcoming MPI-ESM model version will be able to better represent the diurnal cycle.

[10] River runoff is treated interactively in the land hydrology module [*Hagemann and Dümenil-Gates*, 2003] that is embedded in the atmosphere model. The hydrology module applies a higher-resolution (0.5°) grid and contains a river-routing scheme. The resulting freshwater fluxes are interpolated back onto the atmosphere grid and are then passed to the ocean as part of the precipitation field. River discharge is therefore

inserted just over the top grid cell of MPIOM. The mass balance of ice sheets is treated in a simplified way, converting precipitation minus evaporation over the glaciers immediately into surface runoff.

[11] The ocean component, MPIOM, has remained basically unchanged with respect to ECHAM5/MPIOM [*Jungclaus et al*., 2006], and we summarize here only its main features. Details on the model equations and physical parameterizations can be found in *Marsland et al*. [2003]. MPIOM is a free-surface ocean general circulation model formulated on an Arakawa-C grid in the horizontal and a z-grid in the vertical. It solves the primitive equations with the hydrostatic and Boussinesq approximations. Lateral diffusivity is parameterized by an isopycnal formulation based on *Redi* [1982], where the diffusion coefficient varies with grid spacing (proportional to 10^3 m^2 s^{-1} for a 400 km wide grid cell). In addition, tracer transport by unresolved eddies is parameterized following *Gent et al*. [1995]. They formulated the thickness diffusion in terms of an eddy-induced velocity that is added to the tracer advection. In MPIOM, the diffusion coefficient is chosen proportional to the local isopycnal diffusion (250 m^2 s^{-1} for a 400 km wide grid cell). Vertical mixing and diffusion are based on the Richardson-number dependent formulation by *Pacanowski and Philander* [1981]. In addition, turbulent mixing in the ocean mixed layer is assumed to be proportional to the cube of the 10 m wind speed, decaying exponentially with depth and potential density difference to the surface [*Marsland et al*., 2003]. Advection of scalar tracers is computed with a second-order total variation diminishing scheme following *Sweby* [1984], and an advective slope-convection scheme is included for a better representation of statically unstable flow over sills and shelves [*Marsland et al*., 2003]. MPIOM includes a sea-ice model [*Wolff et al*., 1997; *Marsland et al*., 2003; *Notz et al*., 2013] formulated using the viscous-plastic rheology of *Hibler* [1979]. Sea-ice thermodynamics relate changes in sea-ice thickness to a balance of radiant and turbulent atmospheric fluxes, and oceanic heat fluxes. It includes a subgrid-scale treatment of the ice-covered and ice-free part of the grid cell [see *Notz et al*., 2013]. The effect of snow accumulation on sea ice is included, along with snow-ice transformation. Ice formation and melting are accounted for assuming a constant sea-ice salinity of 5 psu.

[12] The model versions used here both apply 40 unevenly spaced levels in the vertical, ranging from 12 m near the surface to several hundred meters in the deep ocean where the bottom topography is represented by a partial-step formulation [*Wolff et al*., 1997]. The first 20 layers are distributed over the upper 700 m. MPIOM applies a conformal mapping grid in the horizontal based on the formulation of *Maier-Reimer* [1997]. Along with the different resolutions (LR and MR), the two versions described here also differ with respect to their conformal mapping grid. One version has two grid poles; this is the GR-grid family described in *Marsland et al*. [2003] and used, for example, by *Haak et al*. [2003], *Jungclaus et al*. [2006, 2008], or *Mikolajewicz et al*. [2007]. The second version uses a newly implemented tripolar (TP) quasi-isotropic grid that has been constructed following *Murray* [1996]. The latter is a combination of a regular Mercator grid south of the Equator and a quasi-isotropic grid to the north of it, in which the North Pole singularity is removed by implementing a line between points over Canada and Siberia. Similar grid configurations can be found in other state-of-the-art ocean and CMIP5 models [e.g., *Griffies et al*., 2011; *Voldoire et al*., 2012]. The TP family of grids is available at 1° (TP1), 0.4° (TP04, as described in this paper), and the eddy-resolving 6-min (TP6M) version described by von Storch et al. (Vertical eddy fluxes of heat, salt, and momentum simulated by the 1/10° STORM OGCM, manuscript submitted to *Journal of Advances in Modeling Earth Systems*, special issue of The Max Planck Institute for Meteorology Earth System Model, hereinafter referred to von Storm, submitted). The GR1.5 grid has two poles, one over Antarctica and one over southern Greenland, and features a nominal resolution of 1.5°, which translates into a grid spacing ranging from 15 km around Greenland to 185 km in the tropical Pacific. The convergence of the mesh size toward the poles thus provides relatively high resolution in the deepwater formation regions around Antarctica and in three regions that are important for northern hemisphere water mass formation: the Labrador Sea, the Nordic Seas, and the Greenland-Scotland Ridge (GSR) with its deepwater conduits [*Jungclaus et al*., 2008]. However, a further refinement toward eddy-permitting resolution would have led to extremely small grid sizes near Greenland, implying the need for very short time steps. While the GR1.5 grid is clearly non eddy-resolving over the world ocean, the TP04 can be classified as "eddy-permitting" for most regions.

[13] Finally, we note that another subset of CMIP5 simulations, the paleointegrations for the last glacial maximum, the mid Holocene, and the last millennium [*Braconnot et al*., 2012] were carried out with another dedicated version of the model, called MPI-ESM-P. This configuration is identical to MPI-ESM-LR with two exceptions: the dynamical vegetation module is not active and the orbital parameters are prescribed rather than calculated from the internal calendar. The representation of oceanic features in the MPI-ESM-P control simulations (also available from the CMIP5 database), such as those documented in this paper, are very similar to the ones in MPI-ESM-LR.

3. Experimental Setup and Spin-Up Procedure

[14] For each model configuration we have performed, a 1000-year control simulation under preindustrial (1850) boundary conditions. These "PICTRL" runs form the reference for the simulations of the instrumental period (1850–2005, a.k.a. "historical" simulations), future scenarios, and idealized climate change experiments [*Taylor et al*., 2012]. A three-member ensemble of "historical" simulations is available for both model configurations, and we use the last 25 years (1980–2005) for comparison with recent near-surface observations. For integrated quantities, interior ocean

properties, and the assessment of low-frequency variability, we focus our analysis on the well-equilibrated 1000 year-long control simulations.

[15] Before a coupled control simulation can be started with a "frozen" model system, a spin-up procedure is necessary to bring the model into equilibrium in terms of radiation balance and to minimize the drift, in particular, in the deep ocean. Changes in the atmosphere physics [*Stevens et al*., 2013], the new land surface and dynamic vegetation schemes, and modified tuning parameters in the coupled system [*Mauritsen et al*., 2012] imply changes in the atmosphere-ocean fluxes compared to the earlier ECHAM5/MPIOM version of the model. In order to arrive at a coupled simulation with as little long-term drift as possible under the constraint of economic use of the available computer time, we start the spin-up simulation not from climatology or an ocean state estimate, but from existing temperature and salinity fields from the CMIP3 preindustrial control experiment. Ocean temperature and salinity fields were readily available for the LR setup, but had to be interpolated onto the TP04 grid for MPI-ESM-MR. During the early phase of the spin up, additional tuning steps turned out to be necessary and interactive vegetation was only switched on after a relatively stable state had been achieved after several hundred years of integration. The spin-up procedure lasted for more than 1900 years in MPI-ESM-LR and, owing to CPU time limitations, 1500 years in MPI-ESM-MR. In both configurations, at least 500 years were run without any further changes before the start of the control simulations. In contrast, the spin up for the CMIP3 model version was only a few hundred years. In addition to the MPI-ESM CMIP5 simulations we will also refer to MPIOM standalone experiments that were carried out in LR, MR, as well as in the eddy-resolving TP6M configurations using atmospheric reanalysis data from the National Center for Environmental Predictions (NCEP) [*Kalnay et al*., 1996] for the period 1948–2010. In contrast to coupled simulations, the NCEP simulations were started after a spin-up time of only a few decades and are therefore much closer to the initial climatology (see von Storch, submitted).

4. Evaluation of the Mean Ocean State

4.1. Ocean Temperature and Salinity

[16] After the spin-up procedure, the atmospheric global mean surface temperature exhibits only little drift around the preindustrial target value of 13.7°C, and the top-of-the-atmosphere imbalance is mainly related to small energy leaks in the atmosphere and the coupling interface [*Mauritsen et al*., 2012]. In the ocean, however, time scales are much longer, and some drift is expected in the deep ocean to prevail over thousands of years.

[17] We compare simulated temperatures and salinities with those from the Polar Science Center Hydrographic Climatology (PHC3). The PHC3 climatology is a blend of the *Levitus et al*. [1998] data with an updated data set for the Arctic from *Steele et al*. [2001]. Deviations with respect to PHC3 in the globally averaged temperature and salinity profiles are similar in both model versions and have retained some of the biases inherited from the CMIP3 solution. Serious biases prevail in particular in the intermediate layers of the ocean. The large errors have evolved during the spin-up and reflect the inability of the model to maintain the correct water mass properties. This appears to be a persistent phenomenon in state-of-the-art climate models [e.g., *Voldoire et al*., 2012; *Danabasoglu et al*., 2012; *Sterl et al*., 2011]. In general, the ocean in MPI-ESM gets too warm and saline at intermediate levels and in the deep ocean whereas it is too cold and fresh in the upper layers. For temperature, biases are considerably smaller in MR, compared to LR and CMIP3 (Figure 1a). Salinity errors (Figure 1c) are relatively similar with some larger errors in the depth-range around 1000 m in MR, possibly caused by overly saline intermediate waters originating in the Red Sea (not shown).

[18] Intermediate-depth biases are often linked to shortcomings in the parameterization of unresolved eddies and/or spurious numerical mixing as an inherent feature of z-level models [e.g., *Delworth et al*., 2012; *Griffies et al*., 2000]. In the more detailed discussion of biases in the Atlantic basin following below, we demonstrate that at least part of the problem can be related to an improper representation of the circulation and the interbasin exchange between Indian Ocean and South Atlantic.

[19] An advantage of our spin-up procedure is that trends over the control runs have been minimized through the long spin-up runs. The linear trends of the order 0.02°C (LR) and 0.05°C (MR) and 0.003 psu per 1000 years (Figures 1b and 1d) are relatively small, compared to those reported from other CMIP5 models [e.g., *Sterl et al*., 2011; *Griffies et al*., 2011]. In fact, the trend in the ECHAM5/MPIOM CMIP3 control simulation was larger by almost 1 order of magnitude (Figures 1b and 1d).

[20] Sea surface temperature (SST) and sea-ice properties are the most important ocean-related quantities in a coupled simulation since they determine the atmosphere-ocean fluxes and their variability. Freshwater fluxes, river runoff, and the resulting sea surface salinities (SSSs) reflect the performance quality of the coupled system. Since the PHC3 climatology represents the modern state of the ocean, we compare the simulated SST from the last 25 years of the historical simulations with the PHC3 climatology (Figure 2). As expected, the present day (1980–2005 average) ensemble means from the historical simulations are warmer than their respective preindustrial control integrations by globally 0.52°C (LR), and 0.58°C (MR) and, therefore, closer to the observed state. Global mean biases for the 1980–2005 average in surface properties and at 1100 m depth relative to the PHC3 data are given in Table 1. The MR model shows generally somewhat smaller errors, both for means and root-mean-square errors (RMSE). The larger mean SST errors in LR can be explained by the slightly colder control state at the beginning of the historical simulation (not shown).

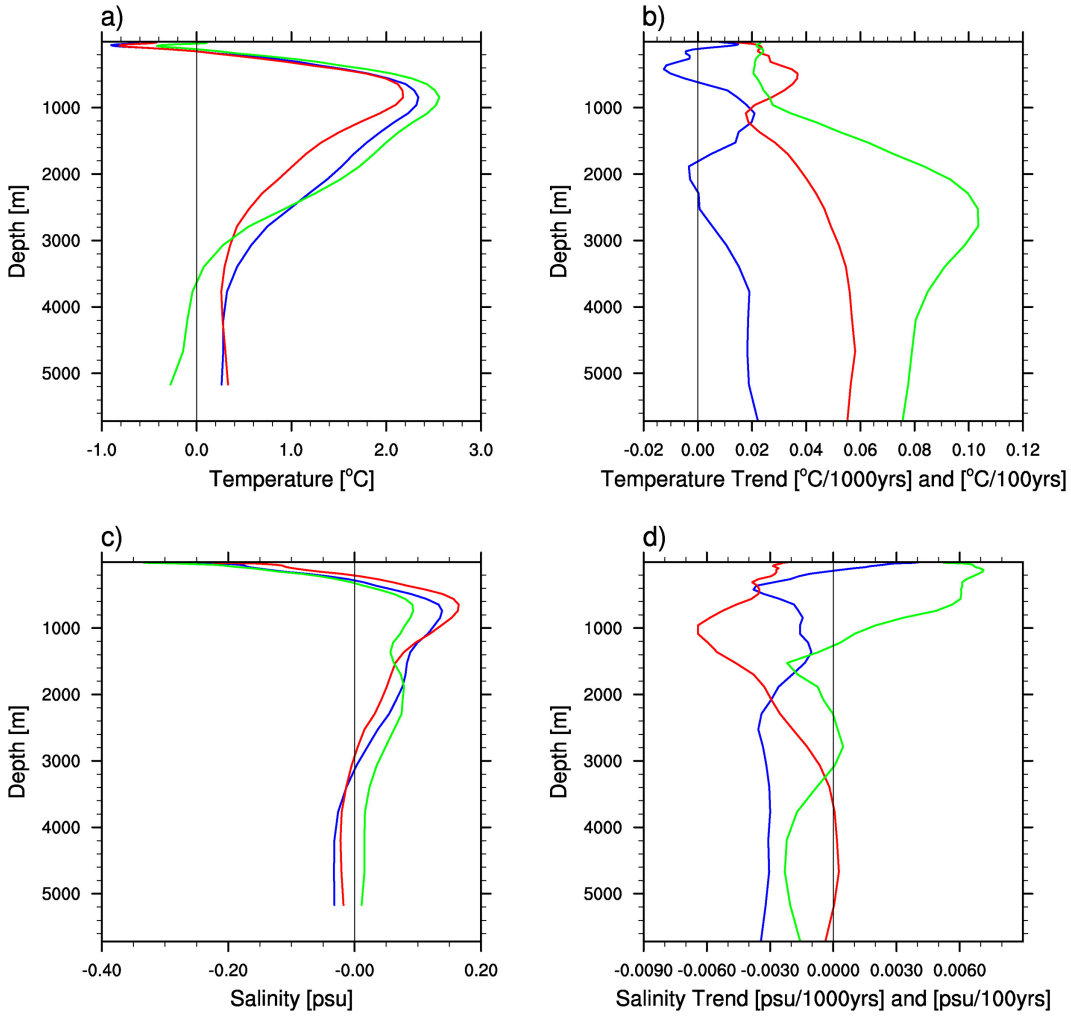

Figure 1. Left column: global time-mean (a) potential temperature bias (°C) and (c) salinity bias (psu) profiles relative to the PHC3 climatology for the (blue) MPI-ESM-LR and (red) MPI-ESM-MR PICTRL simulations, and (green) the ECHAM5/MPIOM CMIP3 control simulation; Right column: long-term drift for global mean (b) temperature and (d) salinity (same colour coding as in Figures 1a and 1c: trends for MPI-ESM are in °C/1000 yr and psu/1000 yr, whereas, for ECHAM5/MPIOM, they are in °C/100 yr and psu/100 yr, respectively).

[22] At the surface, large regions of the world's ocean show biases of less than 1°, and the MR ensemble displays generally slightly smaller errors than the LR ensemble (Figures 2a and 2b). However, there are systematic bias patterns that prevail in both model setups. The largest SST errors are found in the North Atlantic where both model versions produce a too zonally oriented North Atlantic Current (NAC). The resulting cold bias covering the region between the simulated and observed subtropical gyre margin appears to be a persistent feature in state-of-the-art climate models, where lack of resolution prevents a proper representation of the Gulf Stream separation [*Dengg et al.*, 1996]. The problems in the NAC path may, however, also be related to the representation of the deep western boundary current [*Gerdes and Köberle*, 1995; *Bryan et al.*, 2007] and the properties and strengths of the overflows across the GSR [*Danabasoglu et al.*, 2010]. Even though the higher resolution in MR allows for a better representation of key features such as the flow through Florida Strait, there is no improvement in the Gulf Stream/NAC position: the cold bias reaches even further to the north where the "northwest corner" should appear, and the MR realization shows a more pronounced warm bias in the Labrador Sea. Both model versions show a similar surface warm bias in the Nordic Seas. It is likely that a lack of heat loss over the subpolar North Atlantic leads to relatively warmer Atlantic waters in the Nordic Seas [*Swingedouw et al.*, 2012].

[23] The equatorial cold bias in the Pacific, another typical feature of many coupled ocean-atmosphere models, is improved in MR, compared to LR. The area where the bias exceeds 1.5°C is reduced, and the cold tongue does not spread out as far to the west into the Warm Pool. A longstanding problem of coupled models is the proper representation of the upwelling regions at the eastern boundaries of the oceans [e.g., *Randall et al.*, 2007]. *Large and Danabasoglu* [2006] have

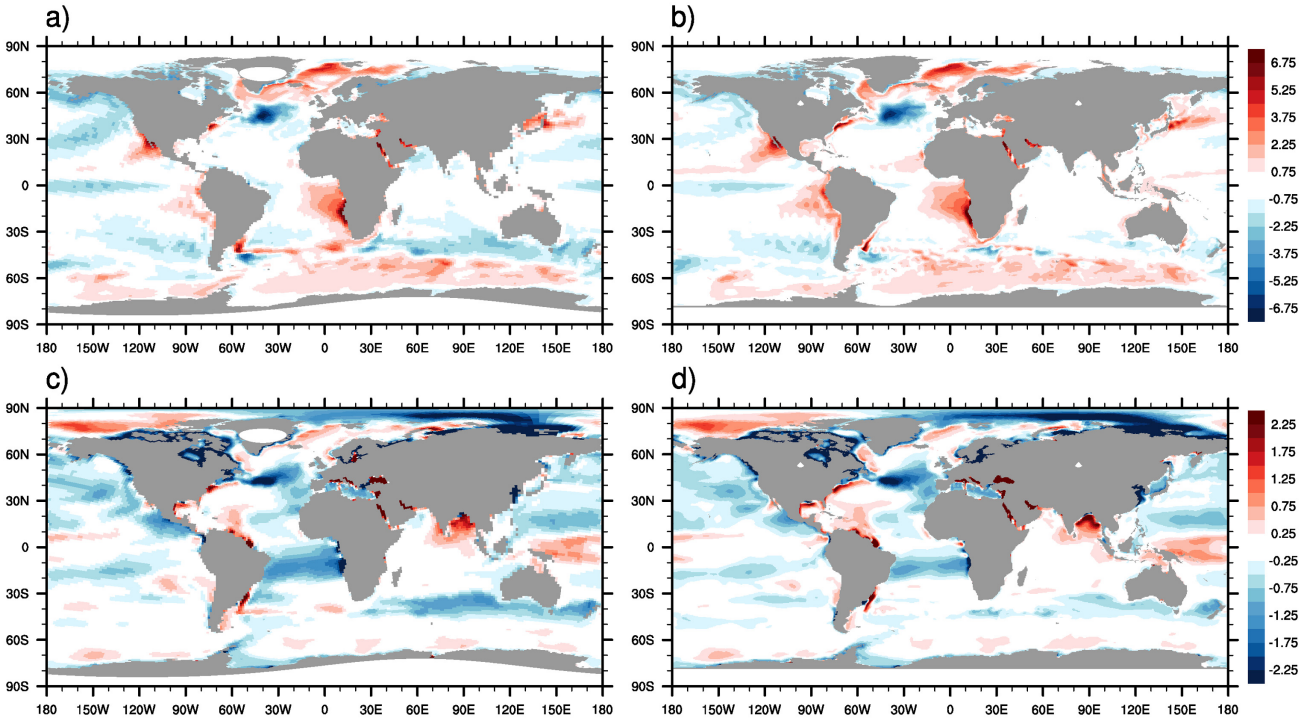

Figure 2. Biases in surface properties for (left column) MPI-ESM-LR, and (right column) MPI-ESM-MR: (a, b) sea surface temperature (°C), and (c, d) salinity (psu) differences between the ensemble means (1980–2005) from the historical experiments and the PHC3 climatology.

investigated these biases in detail and identified a number of interrelated problems typical for a climate model. At relatively coarse resolution, eastern boundary currents and upwelling may be too weak, while erroneous winds and an improper representation of stratocumulus clouds are diagnosed from the atmosphere model. A particular problem is related to the Andes and Sierras, which are not well represented in the T63 atmosphere (see also *Griffies et al.* [2011]). In our simulations, the biases west of Africa and west of Baja California are very similar in LR and MR so that ocean resolution apparently does not improve the boundary currents and upwelling. On the other hand, biases are much smaller in stand-alone ECHAM6 simulations with prescribed SSTs [*Stevens et al.*, 2013], so that the issue of eastern-boundary SST biases clearly remains a problem of the coupled system. Interestingly, the bias pattern is somewhat different in the southeastern tropical Pacific, off the coast of Peru, where the warm bias in simulated SST is smaller in LR than in MR. This feature is related to differences in the upwelling and is presently the subject of further investigations on resolution-dependent differences in the representation of the equatorial dynamics.

[24] The Southern Ocean warm bias seen in both realizations can be associated with an overestimation of downward shortwave radiation into the Polar Regions [*Stevens et al.*, 2013]. This feature remains characteristic of most climate models [*Griffies et al.*, 2011; *Sterl et al.*, 2011]. In our simulation, it goes along with an underestimation with sea-ice coverage, which, in turn, contributes to the warm bias.

[25] There are also considerable differences between the LR and MR simulation in other regions of the Southern Hemisphere: the large cold bias around 40°S in the Indian Ocean sector has largely disappeared in MR due to a more realistic representation of the margin between the subpolar and subtropical gyres. In the western South Atlantic, the error dipole associated with the confluence zone and the pronounced warm maximum at the Brazilian coast near 40°S is reduced in MR, compared to LR. The latter differences, as we show later, are related to different representations of the ocean circulation in the boundary region between Southern Ocean and Atlantic in the different resolutions. The northern part of the Pacific Ocean also

Table 1. Model Minus Observations (PHC3) Area-Weighted Mean and RMSE Differences for SST and SSS, and for the Potential Temperature and Salinity at 1100 m Depth[a]

Index	LR	MR
SST mean bias	−0.41	−0.01
SST RMSE	1.21	1.05
SSS mean bias	−0.22	−0.17
SSS RMSE	0.53	0.49
T_{1100} mean bias	2.34	2.04
T_{1100} RMSE	2.55	2.21
S_{1100} mean bias	0.12	0.11
S_{1100} RMSE	0.18	0.16

[a]Simulated data represent the ensemble mean of the historical simulations for the period 1980–2005. All data were mapped onto a 1° geographical grid prior to the analyses. Temperature and salinity are in °C and psu, respectively.

exhibits relatively strong biases associated with the Kuroshio position. This feature is less pronounced in MPI-ESM-LR. An additional difference between LR and MR is the typical "horse-shoe" pattern in the eastern North Pacific SST pattern. This bias is less pronounced in MR, possibly related to the different bias patterns in the tropical Pacific. A comparison between two NCEP-forced LR and MR stand-alone ocean simulations (not shown) does not produce such differences, indicating that the North Pacific SSTs in the respective coupled simulations may be influenced by the different vertical resolution in the atmosphere, a slightly different tuning of ECHAM6, differences in equatorial SST, or different representations of atmospheric teleconnections in the MR and LR configurations.

[26] Sea-surface salinity biases (Figures 2c and 2d) exhibit rather similar patterns in both LR and MR model configurations. Large deviations from the observation-based climatology are found in the Arctic, with generally too fresh conditions near the Siberian coast and with too salty surface waters in the Canadian Arctic and Beaufort Sea. Part of the fresh bias may be explained by an overestimation of runoff from the Eurasian rivers [*Hagemann et al*., 2013]. The origin of the positive salinity biases in the Canadian Arctic and Beaufort Sea is, however, not clear and may also be related to a summer bias in the observations. In this regard, we also note large (>1 psu) differences between different observation-based data sets, such as PHC3 and the World Ocean Atlas 2009 [*Antonov et al*., 2010] in high northern latitudes. The problems in simulating the correct path of the NAC lead to a negative salinity bias that resembles the cold SST bias in the North Atlantic. Both model versions show a band of too fresh conditions in the subtropical South Atlantic and too salty conditions in the southwestern equatorial Pacific, both related to the displacements of the respective Intertropical Convergence Zones (ITCZs). In the Pacific, these biases are caused by a combination in the shifts of the ITCZ and the South Pacific convergence zone. While the stand-alone version of ECHAM6 driven with observed SSTs produces the well-known "double" ITCZ with associated excess precipitation in the southwestern tropical Pacific, the coupled model simulates much less precipitation directly at the Equator with the largest biases over the warm pool (Andersson, in preparation). In the tropical Atlantic, the shift in the ITCZ leads to excess precipitation on the eastern side of the basin and too little precipitation over the Amazon. The precipitation biases manifest themselves in insufficient Amazon discharge [see also *Hagemann*, 2013; *Grodsky et al*., 2012]. A more comprehensive evaluation with particular focus on precipitation over the oceans is given in an accompanying paper (Andersson, in preparation). For salinity, substantial improvement in MR versus LR occur mainly at the southern exit of the Indian Ocean, also related to the exchange between Indian Ocean and South Atlantic and a more realistic simulation of the position of the northern edge of the Antarctic circumpolar current (ACC) in MR (see section 6.2).

[27] The magnitude and patterns of the surface temperature and salinity biases shown here for the LR configuration are very similar to those from the predecessor CMIP3 model ECHAM5/MPIOM [*Jungclaus et al*., 2006]. Therefore, differences between the CMIP3 and CMIP5 model using the same ocean grid appear less pronounced compared to those between LR and MR. This holds in particular for the errors described above for the South Atlantic and the southern part of the Indian Ocean, and for the salinity biases in the tropical South Atlantic.

[28] Biases in ocean interior water mass structures can be seen in basinwide zonal averages. Errors are typically still large in state-of-the-art ocean models [*Griffies et al*., 2009] and accumulate even more in coupled simulations that are integrated to quasiequilibrium over long spin-up integrations. The current simulations are no exception, and errors of several degrees centigrade reflect problems in parameterization and resolution. Zonal means for the Atlantic and Arctic Ocean, and for the combined Indo-Pacific basin (Figure 3) reveal that the upper layers of the ocean are generally too cold and fresh, whereas the intermediate layers are too warm and too salty. Deepwater masses produced in the Nordic Seas are too warm and saline, and these deviations propagate with the lower limb of the Atlantic overturning circulation into the intermediate and deep ocean. In the upper layers, SST and SSS biases seen in Figure 2 partly penetrate into the upper few hundred meters.

[29] In the Atlantic, the most striking error patterns occur at intermediate depth with maxima near 40°S extending into the Northern Hemisphere at the level of the Antarctic intermediate water (AAIW). Similar errors were found in earlier ocean-only simulations with MPIOM [*Marsland et al*., 2003] and other ocean models [*Griffies et al*., 2009]. Typically, such errors are thought to be related to incorrect interior circulation and tracer advection as well as unrealistic interior mixing, owing to a lack of proper representation of eddy-induced tracer transport [*Griffies et al*., 2009]. In the configurations presented here, the pronounced differences in the LR and MR simulations allow for an identification of the source of the bias. In a set of ocean-only simulations (not shown), the error near 40°S and 1000 m depth is established very quickly after the start of these experiments using the GR1.5 grid and can clearly be related to advection of warm and salty water from the Indian Ocean. The respective simulations with the TP04 (eddy permitting) and TP6M (eddy resolving) model configuration demonstrate that the resolution-dependent representation of the Agulhas current system, its retroflection, and the associated transfer of salt and heat (see section 6.2) is responsible for the larger mismatch at lower resolution. In fact, the bias is further reduced in the eddy-resolving TP6M ocean-only run.

[30] In both configurations displayed in Figure 3, the error patterns stretch out to the north at the depth of the AAIW but are much more pronounced in LR. Moreover, in LR, there is another local maximum in the salinity bias near 30°N that can be associated with the impact of warm and saline Mediterranean waters. While the mass transport of the exchange flow through

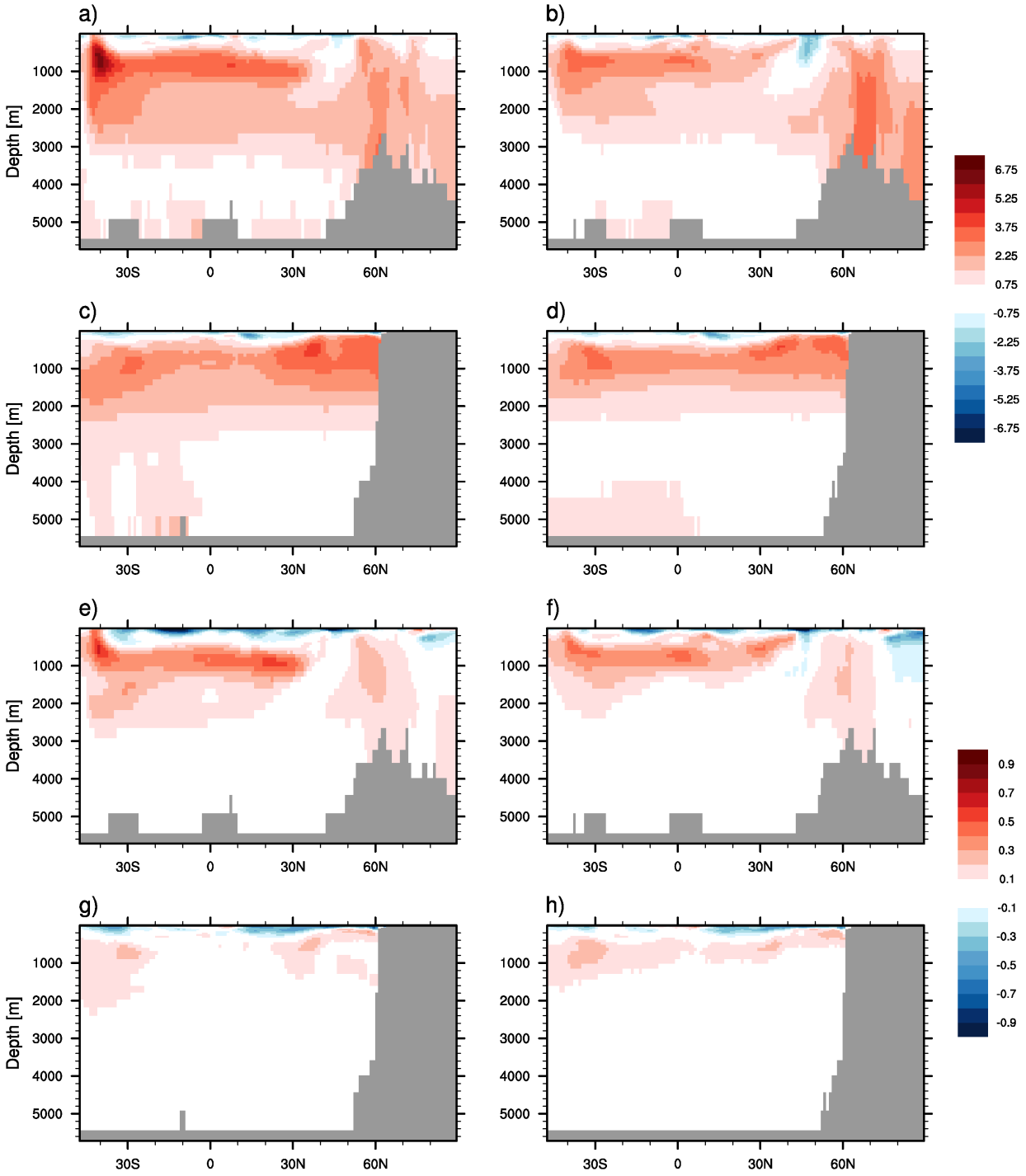

Figure 3. Atlantic Ocean (a, b, e, f) and Indo-Pacific (c, d, g, h) zonal averages for (a, b, c, d) potential temperature, and (e, f, g, h) salinity differences between (left columns) MPI-ESM-LR, and (right column) MPI-ESM-MR PICTRL simulations and the PHC3 climatology.

the Strait of Gibraltar is of similar strength in both setups (Table 2), the Mediterranean water is distributed differently by the large-scale circulation in the Atlantic (not shown). In MR, part of the Mediterranean outflow is flowing northward along the European continental shelf, whereas the warm and saline water masses in LR almost entirely spread out in southwesterly direction into the open Atlantic. The too zonal path of the NAC leads to a cold and fresh bias in the upper ocean between 40 and 50°N. The larger warm bias in the MR simulation around 60°N and to the north of the GSR is not compensated for by salinity errors and leads to reduced densities in the Nordic Seas in this setup. As shown in section 4.6, shallower mixed-layer depths

Table 2. Transports (Sv) Through Passages From Long-Term Means of the PICTRL Simulations of MPI-ESM-LR and MPI-ESM-MR Together With Observational Estimates[a]

Section	LR	MR	Observations	Reference
Drake Passage	169	182	137±8	*Cunningham et al.* [2003]
Indonesian Throughflow	16.9	15.7	11.6–15.7	*Gordon et al.* [2010]
Bering Strait	0.72	1.0	0.8–1	*Woodgate et al.* [2006]
Denmark Strait				
Total	5.5	6.5	4.6	*Hansen et al.* [2008]
Overflow >27.8	3.7	2.5	3–3.	*Macrander et al.* [2005]
Iceland-Scotland				
Total	5.2	5	4.8	*Hansen et al.* [2008]
Overflow > 27.8	3.1	3.5	3.4	
Strait of Gibraltar				
Inflow	1.1	1.0	0.78	*Tsimplis and Bryden* [2000]
Outflow	1.0	0.95	0.67	
Mozambique Channel	25.1	19	5–26	*DiMarco et al.* [2002]
Florida Current		16	31.7	*Kanzow et al.* [2010]

[a]If not specified otherwise, the numbers represent the total (depth-integrated) barotropic transport.

(MLDs) in the MR realization indicate that there is less heat release to the atmosphere in the sinking regions. Since the strength of the overflow across the GSR is determined in part by the density contrast between the basins, the temperature mismatch is probably also responsible for a weaker overturning circulation in the northern North Atlantic in MR (see section 4.3).

[32] The error patterns in the Indo-Pacific basin (Figures 3 c, 3d, 3g, and 3h) show much less differences between the two model versions. Slight improvement is seen in the MR representation of temperatures in the North Pacific while errors in the tropics appear to be a bit more pronounced. Therefore, while better resolving the exchange flow between Indian Ocean and South Atlantic has improved the biases in the Atlantic, the general problem of middepth biases known from other models, remains. *Delworth et al.* [2012] compared coupled simulations at roughly 1°, 0.25°, and 0.1° resolution and found a deterioration of the bias magnitude in the eddy-permitting solution. They related the subsurface drift in that model to insufficiently resolved mesoscale eddies (the Gent-McWilliams parameterization was switched off). In our model, retaining GM, though with a relatively low coefficient, has allowed us to arrive at a similar bias in both model versions.

4.2. Large-Scale Ocean Circulation

[33] The large-scale horizontal circulation is described in terms of the barotropic streamfunction (BSF) in Figure 4. As MPIOM is a free-surface model, BSF is diagnosed from the vertically integrated horizontal velocities at each time step. Both model configurations reproduce the well-known features of the oceanic gyres and large-scale current systems. In the North Atlantic, subpolar gyre maximum values of BSF to the south of Greenland are 37 Sv in MR and 28 Sv in LR (1 Sv = 10^6 m^3 s^{-1}), bracketing the observational estimate of 34 Sv given by *Clarke* [1984]. Both model configurations feature a maximum subtropical gyre BSF of about 50 Sv, comparable to the estimate of 48 Sv by *Johns et al.* [1995]. In the Pacific, the subtropical gyre associated with the Kuroshio has a maximum of about 80 Sv to the south of Japan in the LR and about 60 Sv in MR configurations, whereas estimates derived from altimeter products give about 42 Sv [*Imawaki et al.*, 2001]. However, the peak value in the model is determined by a relatively small recirculation cell. Observations [e.g., *Jayne et al.*, 2009] indicate peak values of the Kuroshio transport of up to 114 Sv. Important differences between the two configurations appear at the boundary between Southern Ocean and South Atlantic and the Agulhas region south of Africa. The Agulhas current is a boundary current that flows westward around the Cape of Good Hope before retroflecting to the south and then recirculating eastward. In the LR configuration, there is much too little retroflection, and the Indian Ocean subtropical gyre extends far into the South Atlantic, forming a huge "super gyre." The zero line of the BSF to the south of Africa, which forms the boundary between the Agulhas system and the ACC, is found several degrees further to the south so that the Indian Ocean is more connected to the South Atlantic. As a result, the South Atlantic subtropical gyre is much stronger in LR (90 Sv) than in MR (62 Sv) and much higher than in estimates from hydrographic observations such as the ∼30 Sv reported by *Peterson and Stramma* [1991]. The connection between Indian Ocean and South Atlantic is an important component of the global thermohaline circulation [e.g., *Gordon*, 1986] and has received increased attention in recent years [e.g., *Beal et al.*, 2011]. The resolution-dependent differences in the LR and MR configurations will therefore be further explored in section 6.2.

[34] In the western South Atlantic, the Brazil current separation and the Malvinas confluence is also affected by the different northward extensions of the ACC in LR and MR. The reduced SST bias here (Figure 2) indicates a better representation in MR compared to LR.

[35] As shown in Table 2, the total depth-integrated transports through important passages are largely simulated within the uncertainty of the observational estimates. The transport of relatively fresh water from the Pacific into the Arctic is one fundamental ingredient for the freshwater budget of the Arctic and the Atlantic Ocean. The two model solutions (0.7 Sv in LR and 1 Sv in MR) bracket the observational estimate of 0.8 Sv,

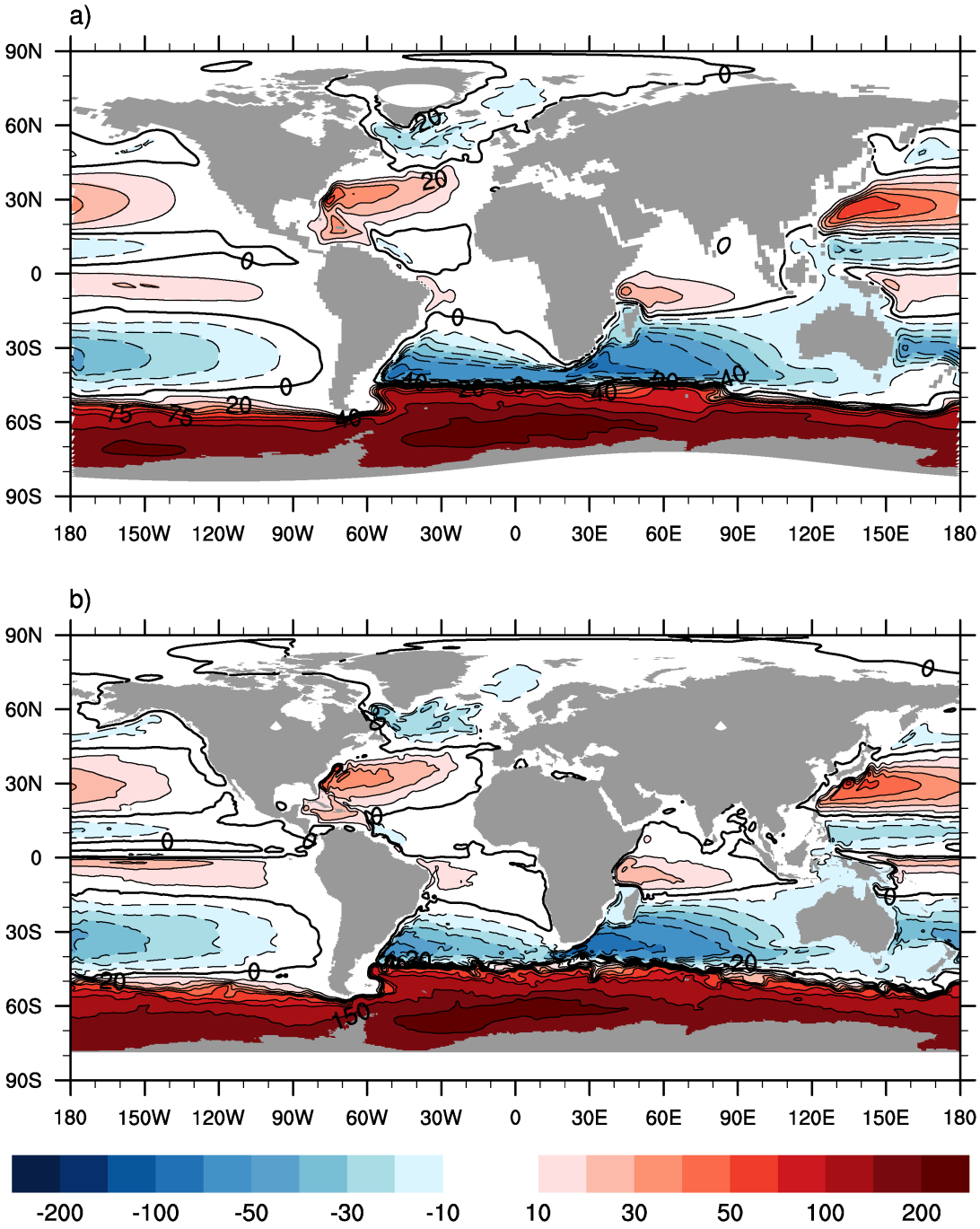

Figure 4. BSF (Sv) from the PICTRL simulations (a) MPI-ESM-LR and (b) MPI-ESM-MR; contour intervals are 0, 10, 20, 30, 40, 50, 75, 100, 150, and 200 Sv; analogous for negative values.

even though the channel, as represented by one grid box in the Arakawa-C grid, is too wide in the LR configuration. The Nordic Seas exchange water masses with the Atlantic through the different openings of the GSR. The total flux through Denmark Strait appears to be slightly overestimated in comparison with observations. The combined depth-integrated flow between Iceland and Scotland is close to 5 Sv in both models, consistent with the transport scheme provided by *Hansen et al.* [2008, Figure 1.12]. However, the distribution between the openings to the east and west of the Faroe Island is realized somewhat differently in the two model setups. While the transport is almost equally divided between the two openings in LR, this is not the case in MR where we find much higher transports between Iceland and the Faroes (not shown). The latter indicates different pathways of the Atlantic Water branches that are likely caused by the slightly different Subpolar Gyre geometries. Going further south in the Atlantic, the GR1.5 grid does not contain a Florida Strait (Figure 4),

whereas, in the TP04 grid, it is possible to obtain a transport between Florida and the Bahamas of 16 Sv. Data from the RAPID program monitored a transport of 31.7 Sv using a submarine cable between Florida and the Bahamas [*Kanzow et al.*, 2010]. In the model, however, the distribution of the flow to the east and west of the Bahamas is not distinguishable.

[36] The Indonesian throughflow forms another important part of the global thermohaline circulation and the models simulate only slightly higher transports (16.9 Sv in LR and 15.7 Sv in MR) than the observations (11.6–15.7 Sv). Although there are large differences between the Indian Ocean subtropical gyre systems in the two setups, the simulated flows through the Mozambique Channel (25 Sv in LR and 19 Sv in MR) are in agreement with the range of observations (5–26 Sv) [*DiMarco et al.*, 2002]. The Drake Passage transport is clearly too strong compared to observations; it reads 169 Sv in LR and 185 Sv in MR. *Cunningham et al.* [2003] gave a value of 137 ± 8 Sv and *Nowlin and Klinck* [1986] estimated 134 Sv with an uncertainty range of 14 Sv. Overestimating the Drake Passage transport may be caused by insufficient representation of the eddy dynamics in the ACC but could also be related to overly strong winds or errors in the representation of water masses. Ocean-only experiments driven by NCEP atmospheric forcing overestimate the Drake Passage transport even more: both LR and MR configuration simulate transports of almost 200 Sv. Probably therefore, the too strong ACC is caused by an overestimation of the density gradient across the ACC. *Gent et al.* [2001] have identified several ingredients setting the ACC strength in a model, among them bottom topography and the choice of the eddy and background diffusivity. However, more focused sensitivity experiments would be necessary to explain the fact that the MR model produces a stronger ACC. We note that the ACC strength in ECHAM5/MPIOM (165 Sv) was very similar, indicating no improvement between the CMIP3 and CMIP5 realizations.

[37] We also include in Table 2 the flow of relatively dense waters that form the overflows across the GSR. The $\sigma_\Theta = 27.8$ isopycnal is traditionally taken to define the interface of the dense overflow waters crossing the GSR mainly through Denmark Strait and the Faroe Bank Channel. We diagnose a considerably stronger overflow in Denmark Strait in the LR (3.7 Sv) compared to the MR (2.5 Sv) configuration. While both results bracket the often quoted estimate of 2.9 Sv by *Ross* [1984], the higher transport in the LR model agrees better with the more recent measurements of *Macrander et al.* [2005] who diagnosed a mean transport of 3–3.5 Sv from a 5 year long campaign. In the Faroe Bank Channel, both models simulate an overflow transport exceeding 3 Sv (LR 3.1 Sv; MR 3.5 Sv), a bit higher than the observational estimate of about 2 Sv [*Hansen and Østerhus*, 2007]. However, the simulated overflow to the east of Iceland occurs mainly in the Faroe Bank Channel, whereas observations suggest an additional 1 Sv contribution from various small channels between Iceland and the Faroes [*Dickson and Brown*, 1994]. Thus, the total strength of the outflow of dense water from the Nordic Seas between Iceland and Scotland is simulated relatively well. Comparing the overflow transports with those from ocean-only experiments (not shown) confirms that MPIOM produces considerably less overflow in Denmark Strait in the MR setup compared with the LR configuration even if the properties of the northern source waters are similar. This points to a better representation of the overflow conduit in the LR configuration. In terms of grid resolution, the LR (GR1.5) model, owing to the proximity of the northern grid pole over Greenland [see *Jungclaus et al.*, 2008, Figure 22.3], resolves the Denmark Strait better than the more homogeneous MR (TP04) configuration, whereas the region to the east of the Faroe Islands is represented rather similarly.

4.3. Meridional Overturning Circulation

[38] The large-scale meridional overturning circulation (MOC) is an important component of the climate system as a carrier of heat and freshwater. In the Atlantic, the MOC is responsible for the northward heat transport throughout the basin. The MOC circulation is represented by the clockwise rotating North Atlantic Deep Water (NADW) cell and the counterclockwise rotating Antarctic Bottom Water (AABW) cell. Both LR and MR (Figure 5) configurations exhibit a similar

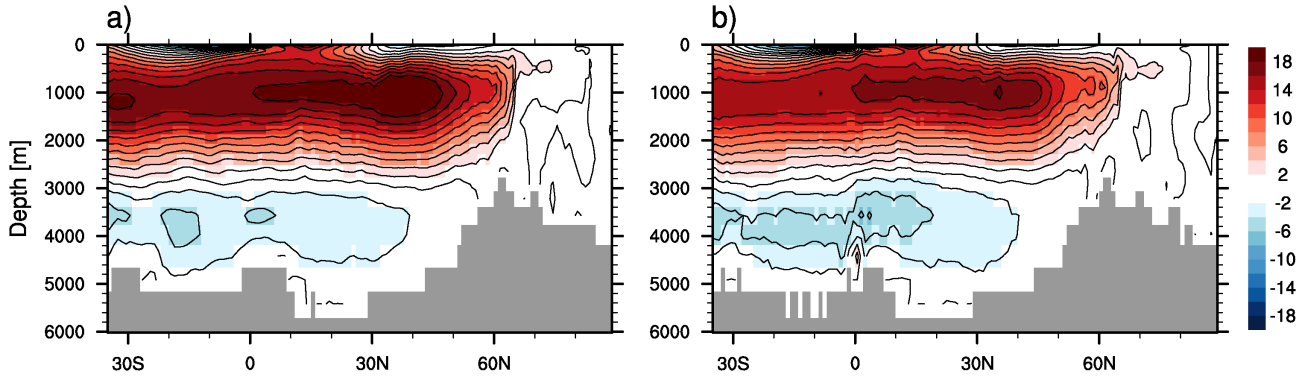

Figure 5. Atlantic meridional overturning streamfunction (Sv) from the PICTRL simulations (a) MPI-ESM-LR, and (b) MPI-ESM-MR; contour intervals are 2 Sv.

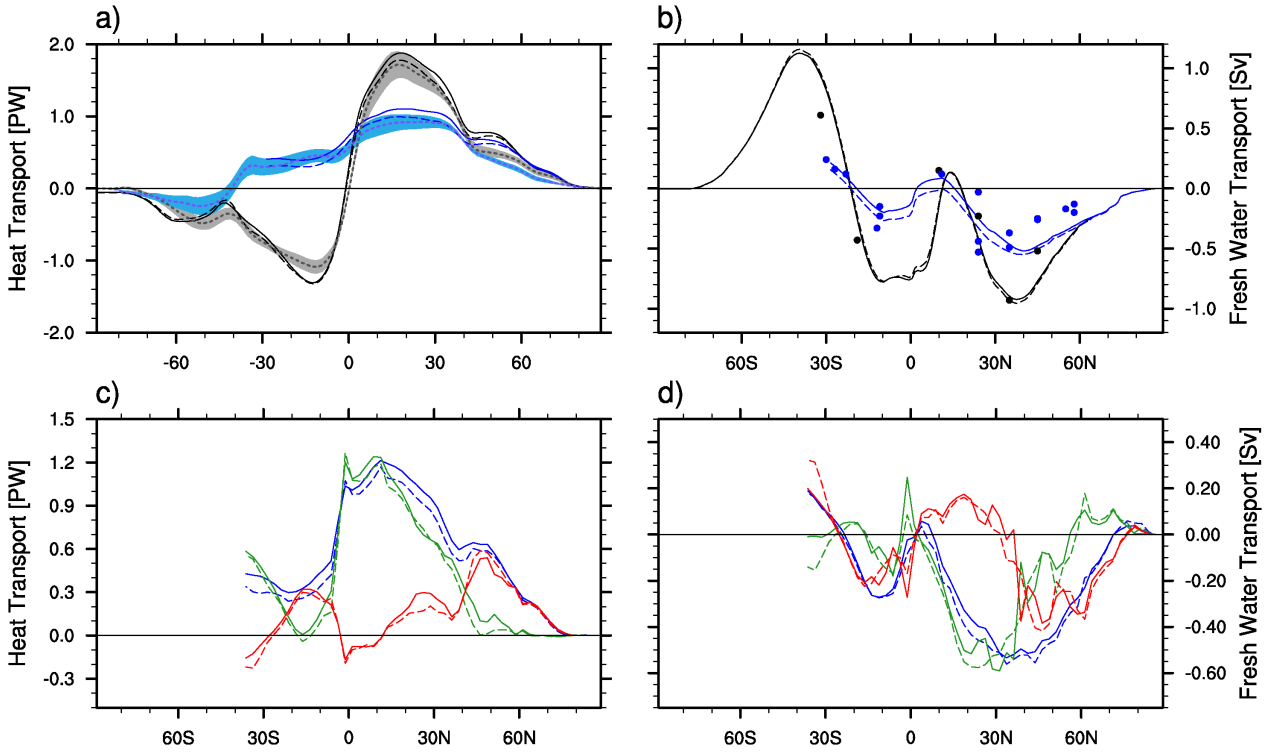

Figure 6. Meridional (left column) heat (PW), and (right column) freshwater (Sv) transport for the global ocean and the Atlantic Ocean from the PICTRL simulations (solid lines) MPI-ESM-LR, and (dashed lines) MPI-ESM-MR. The upper row displays heat and freshwater transports implied by the net ocean-atmosphere fluxes. For the heat transports, the dotted line and the shadings depict the observation-based estimates by *Trenberth and Fasullo* [2008]. For the freshwater transports, dots indicate observational estimates from various sources compiled in *Wijffels* [2001]. The lower row shows the (blue) total advective transports in the Atlantic, decomposed into (green) overturning, and (red) gyre component.

structure with the zero line between the two cells at approximately 3000 m, a maximum of the NADW cell between 35°N and 40°N and an extension of the clockwise cell into the Nordic Seas (Figure 5). The simulated streamfunctions also resemble those from the CMIP3 model [*Jungclaus et al.*, 2006, Figure 6] with slight improvement in the AABW strength. Generally, MPI-ESM-MR features a weaker NADW and a stronger AABW cell. The simulated maxima of the NADW cell at 26.5°N in the North Atlantic read 19 Sv for LR and 16.7 Sv for MR at 1000 m depth and bracket the observational estimate of 18.7 Sv obtained from the 4 year RAPID campaign [*Kanzow et al.*, 2010]. The data from the RAPID array indicate also a similar depth of the NADW maximum, but the boundary between NADW and AABW cell is considerably deeper (between 3500 and 4000 m) in the observations, indicating that NADW is not dense enough in the simulations. *Danabasoglu et al.* [2010, 2012] found an improved depth profile for experiments including an overflow parameterization, which would indicate that the water mass properties originating in the Nordic Seas are essential for setting the depth of the Deep Western Boundary Current. The maximum strength of the AABW cell in the RAPID data at 26.5°N [*Kanzow et al.*, 2010, Figure 5] is about −2 Sv, where our simulations show −2.8 Sv in LR and −3.4 Sv in MR. In the South Atlantic, the stronger inflow of AABW as simulated by MPI-ESM-MR appears to be more in accordance with the inverse-model result by *Ganachaud and Wunsch* [2003] of about 6 Sv. *Talley et al.* [2003] calculate about 8 Sv from absolute geostrophic velocities based on hydrographic data. Both estimates come, however, with relatively large uncertainty owing to sampling problems.

[39] The comparison of the maximum of the NADW cell as a function of latitude of the two model setups (not shown) confirms that the strength of the overturning is weaker in MR throughout the Atlantic up to ~60°N. NADW is to a large part fed by the overflow across the GSR [*Dickson and Brown*, 1994]. As described in the previous section, the MR configuration produces less overflow transport, in particular, in Denmark Strait. Moreover, a more detailed inspection of overflow water mass properties reveals that the overflows are also slightly less dense in MR (see above). After leaving the overflow conduits, the dense waters descend on the continental slopes and entrain considerable amounts of ambient waters, roughly doubling their volume transport in idealized overflow models. According to *Price and Baringer* [1994], the amount of entrainment depends on the flow velocity and the density contrast in a way that a denser

overflow entrains more ambient fluid. Therefore, the weaker overturning in the MR configuration can in part be explained by differences in the water mass properties that form the dense water reservoir in the Nordic Seas. The other part seems to be related to a different representation of Denmark Strait in the respective grids. The globally lower-resolution model gives a better representation of the dense overflow in terms of transport in this particular region of grid-size convergence.

4.4. Heat and Freshwater Transports

[40] Another key quantity is the meridional ocean heat transport. In both models, the implied global heat transports (Figure 6a), obtained from the residual atmospheric heat fluxes, agree well with estimates that are based on satellite retrievals of adjusted radiances and atmospheric reanalyses [*Trenberth and Fasullo*, 2008; *Fasullo and Trenberth*, 2008]. In the Atlantic, the MPI-ESM-LR heat transport (max 1.1 PW, 1PW $=10^{15}$W) exceeds this observation-based estimate with its maximum slightly below 1 PW. However, *Ganachaud and Wunsch* [2003] report 1.27 ± 0.15 PW from inverse calculations and the recent estimate from the RAPID campaign reads 1.3 PW [*Johns et al.*, 2011]. The maximal transport in MPI-ESM-MR is about 0.95 PW, somewhat smaller than in LR. Interestingly, this does not appear to be related only to the weaker overturning cell. Decomposing the advective heat transports into the zonally averaged (MOC) and deviation-from-the-zonal-average (gyre) components for the Atlantic (Figure 6c), shows nearly identical MOC components between 20°N and 35°N and a weaker gyre contribution in MR.

[41] The global freshwater transports, as implied from the atmosphere to ocean fluxes (Figure 6b), are in reasonable agreement with observational estimates [*Wijffels et al.*, 2001]. As the latter are sparse and associated with large uncertainties, we can deduce from the observations mainly the latitudes of sign changes and approximate maxima and minima. Overall, we see a slightly better agreement compared to the ECHAM5/MPIOM model [*Jungclaus et al.*, 2006, Figure 7]. Differences between the two CMIP5 configurations are small. For most of the Atlantic, this holds also for the MOC and gyre components of the advective transports (Figure 6d). Interestingly, there is a deviation again at the southern boundary of the Atlantic. Both model configurations agree on a total freshwater import into the South Atlantic of about 0.2 Sv, consistent with

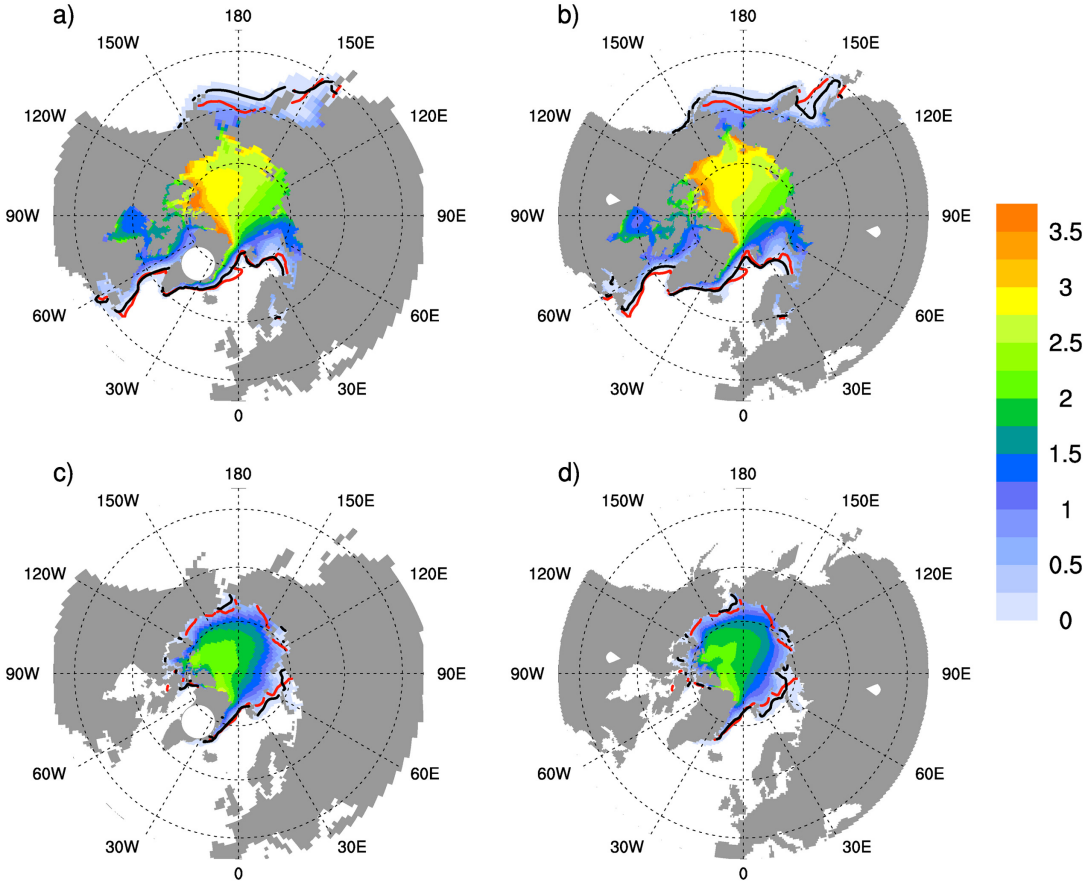

Figure 7. Sea ice thickness (m) for the Northern Hemisphere from the historical simulations (1980–2005 ensemble mean) for (left column) MPI-ESM-LR, and (right column) MPI-ESM-MR; (a, b) depict March, and (c, d) September conditions. The black lines indicate the simulated ice extent, defined by 15% ice concentration, red lines show the respective ice extent derived from observational data (NSIDC).

the notion of the Atlantic as an evaporative basin, but the relative contribution of the subcomponents is different. At 34°S, the overturning component is clearly negative in MR, whereas it is close to zero in LR and the gyre components differ accordingly (see section 6.2).

4.5. Sea Ice

[42] Sea ice modifies the heat, momentum, and freshwater exchanges between ocean and atmosphere in (temporarily) ice-covered regions. Local melting and freezing and advective transports determine the sea-ice budget. A more detailed account of the sea-ice evolution in the Arctic and a comparison between the respective representations in the CMIP3 and CMIP5 models is given in a separate paper by *Notz et al.* [2013]. In addition, the sensitivity of the simulations to changes in the model parameterization of sea-ice geometry is discussed by *Mauritsen et al.* [2012]. Here we document only the most general features reflecting on the ability of the model to reproduce a realistic ice cover and thickness distribution. Regarding Arctic sea-ice coverage over the years 1980–2005, MPI-ESM shows good agreement with the observed ice extent obtained from NOAA/NSIDIC [*Meier et al.*, 2011] (Figure 7). We diagnose for the MPI-ESM historical simulations marked improvements compared to the CMIP3 predecessor model that was evaluated by *Koldunov et al.* [2010]. MPI-ESM produces, in general, less summer sea ice, in particular, in regions where ECHAM5/MPIOM overestimated the ice cover: in the Laptev Sea, the East Siberian Sea, and the Canadian Archipelago. Modeled ice extent from MPI-ESM matches observations now almost everywhere, with the exception of slightly underestimated summer ice cover in the Kara Sea. In winter, notable differences between model and observations are a too small modeled sea-ice extent in the Odden ice tongue and in the Sea of Okhotsk, and a too large sea-ice extent south of the Bering Strait. In contrast to ice extent, the sea-ice thickness distribution is still a challenging quantity to observe, and only recently has it been possible to compile observational data from satellites into a sea-ice reanalysis framework [*Lindsay and Zhang*, 2006]. The Pan Arctic Ice-Ocean Modeling and Assimilation System (PIOMAS) [*Schweiger et al.*, 2011] allows for an assessment of ice thickness over longer time and space scales in the Northern Hemisphere. PIOMAS data suggest a mean annual ice thickness of 2.5–3.3 m for the Arctic and a typical winter ice distribution with the thickest ice (exceeding 3.5–4 m) to the north of Greenland and the Canadian Archipelago. The MPI-ESM modeled distribution of sea ice thickness with the highest accumulation to the north of Greenland and the northern exit of the Canadian Archipelago agree well with the PIOMAS reanalysis [*Schweiger et al.*, 2011, Figure 6]. The simulated sea-ice distribution, extent, and thickness are remarkably similar in the LR and MR configurations. The improvements compared to the CMIP3 simulations must be sought in the atmosphere model. For the higher northern latitudes, the evolution from a low-top model to a high-top model including the stratosphere appears to be most important, while further enhancing the vertical resolution in the atmosphere model from 47 levels in LR to 95 levels in MR leads to a better representation of variability features (e.g., quasi-biannual oscillation [*Stevens et al.*, 2013]).

[43] While the annual cycle of Arctic sea ice evolution has been improved, Southern Hemisphere sea ice is generally underestimated in MPI-ESM (Figure 8). The seasonal cycle of sea ice area is less well simulated than in the CMIP3 system [*Jungclaus et al.*, 2006, Figure 4]. This seems to be related to issues in the atmospheric pressure distribution, with a—compared to observations—too strong modeled low-pressure system over the Amundsen Sea and a significantly different air-pressure distribution over the Weddell Sea.

4.6. Mixed-Layer Depth

[44] The surface mixed layer is deepened by wind-induced mixing, Ekman subduction, and mixing of gravitationally unstable water columns. Such convective water mass formation is important in the formation of NADW and AABW, but also for mode waters such as the Subantarctic Mode Water (SAMW). Convectively active regions can be identified by the maximum depth of mixing attained during an annual cycle. The MLDs are calculated here using a potential density criterion of 0.125 kg m^{-3}. For each grid point, Figure 9 depicts the annual maximum monthly MLD obtained from the 1000 year control integrations. Overall, MPI-ESM-LR and -MR produce similar patterns of convectively active regions. One important region for NADW formation is the Labrador Sea. The LR configuration features deep convection more confined to the interior Labrador Sea, which is in better agreement with observations [*Pickart et al.*, 2002]. As mentioned earlier in the discussion of the subpolar gyre circulation, the higher resolution in the Atlantic does not help to better reproduce the pathway of the NAC in MR. On the contrary, there is a broader subpolar gyre in MR with somewhat less realistic circulation also in the Irminger and Labrador Seas. Moreover, the grid resolution near the southern tip of Greenland is higher in LR than in MR owing to the grid convergence, so that the boundary current in the Labrador Sea is simulated more accurately in LR (not shown). The centers of convection in the Nordic Seas are simulated similarly in both model configurations. In general, the MR model produces considerably shallower MLDs in the northern sinking regions, indicating less-intensive convection and less heat release to the atmosphere, which could be responsible for a more pronounced warm bias in the northern North Atlantic (Figure 3). However, as has been discussed with respect to the strength of the overflows across the GSR, the depth of the mixed layer alone is not a good measure of the deep water production that eventually feeds the NADW via the overflows across the GSR.

[45] In the Southern Hemisphere, deep MLDs around 40°S indicate the pycnostads associated with SAMW formation [*Talley et al.*, 2011]. Estimates based on observations [e.g., *Kara et al.*, 2003] indicate a band of deep mixed layers extending along much of the

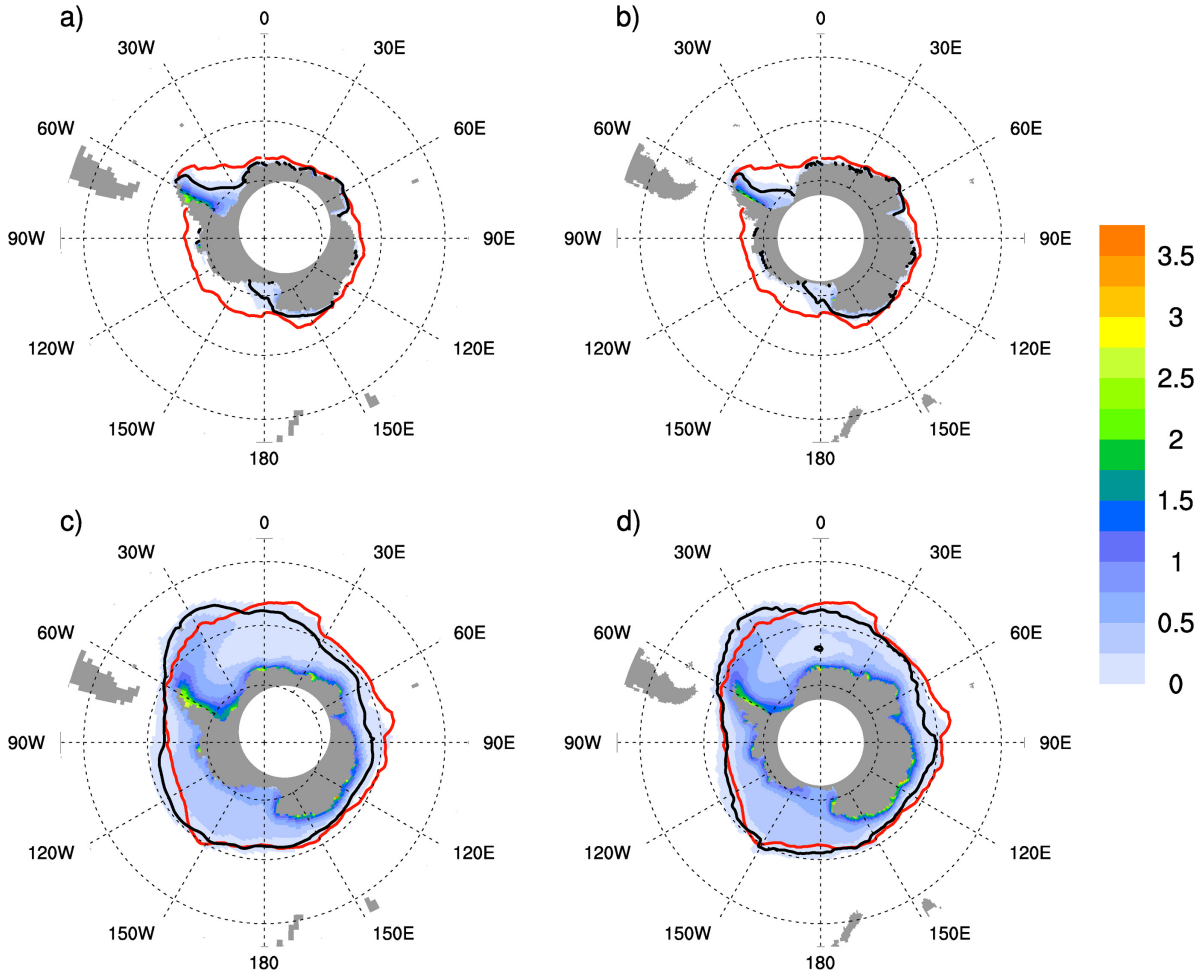

Figure 8. Sea ice thickness (m) for the Southern Hemisphere from the historical simulations (1980–2005 ensemble mean) for (left column) MPI-ESM-LR, and (right column) MPI-ESM-MR; (a, b) depict March, and (c, d) September conditions. The black lines indicate the simulated ice extent, defined by 15% ice concentration, red lines show the respective ice extent derived from observational data (NSIDC).

northern flank of the ACC in the Indian and Pacific Ocean. The simulations reproduce this feature in general, but considerable differences can be seen in the Indian Ocean. In MPI-ESM-LR the deep MLDs in the Indian Ocean are almost absent or shifted to the southern flank of the ACC. Compared to *Kara et al.* [2003] and the ocean reanalysis by *Carton and Giese* [2008] MPI-ESM-MR reproduces shape and magnitude of SAMW-related MLDs in the southern Indian Ocean more realistically than MPI-ESM-LR. The regions of improved MLDs are also characterized by a better representation of SST and SSS (Figure 2). We notice also differences in the western South Atlantic and to the west of Cape Horn, but the information from observations and reanalysis does not allow for a judgment which model configuration does better. Adjacent to Antarctica, both configurations simulate extremely deep mixed layers and active convection down to the deep ocean in the Weddell Gyre, but also in the Ross Sea. Although deep convection has been observed in the Weddell Sea [*Gordon*, 1978], such observations are scarce and both model setups are very likely to overestimate open ocean convection, while they are underestimating dense water formation on the shelves surrounding Antarctica [e.g., *Marsland et al.*, 2004]. This discrepancy might be responsible for the general overestimation of the ACC in both model versions.

5. Variability in the Coupled System

[46] The main focus of the present manuscript is a documentation of the mean state of the ocean in the MPI-ESM integrations. Nevertheless, we include here two aspects of variability that are important for the coupled system: The El Niño Southern Oscillation (ENSO), and the decadal to multidecadal variability of heat transports in the North Atlantic.

5.1. ENSO

[47] Compared to the CMIP3 model, the representation of ENSO in our CMIP5 simulations has clearly improved in terms of the strength of the variability. The amplitude, the primary metric of ENSO measured here

by the standard deviation of the Niño3 (5°S–5°N, 150°W–90°W), Niño3.4 (5°S–5°N, 170°W–120°W), and Niño4 (5°S–5°N, 160°E–150°W) SST anomalies (Table 3), has decreased considerably, for example, for Niño3.4 from an overly strong 1.26°C in ECHAM5/MPIOM to a level close to the 0.76°C from observations in LR (0.75°C), while being slightly weaker for the MR configuration (0.67°C). While the convergence of ENSO amplitude toward the observed range is encouraging, an examination of the physical feedbacks responsible for ENSO development reveals that the new models also suffer from an underestimation of the Bjerknes feedback that tends to be compensated by a too-low thermal damping effect [*Guilyardi et al.*, 2012].

[48] The shape and amplitude of the ENSO power spectrum are relatively well simulated by the new model (Figure 10). As in the observations, the modeled ENSO exhibits a rather broad spectrum between 2.5 and 6

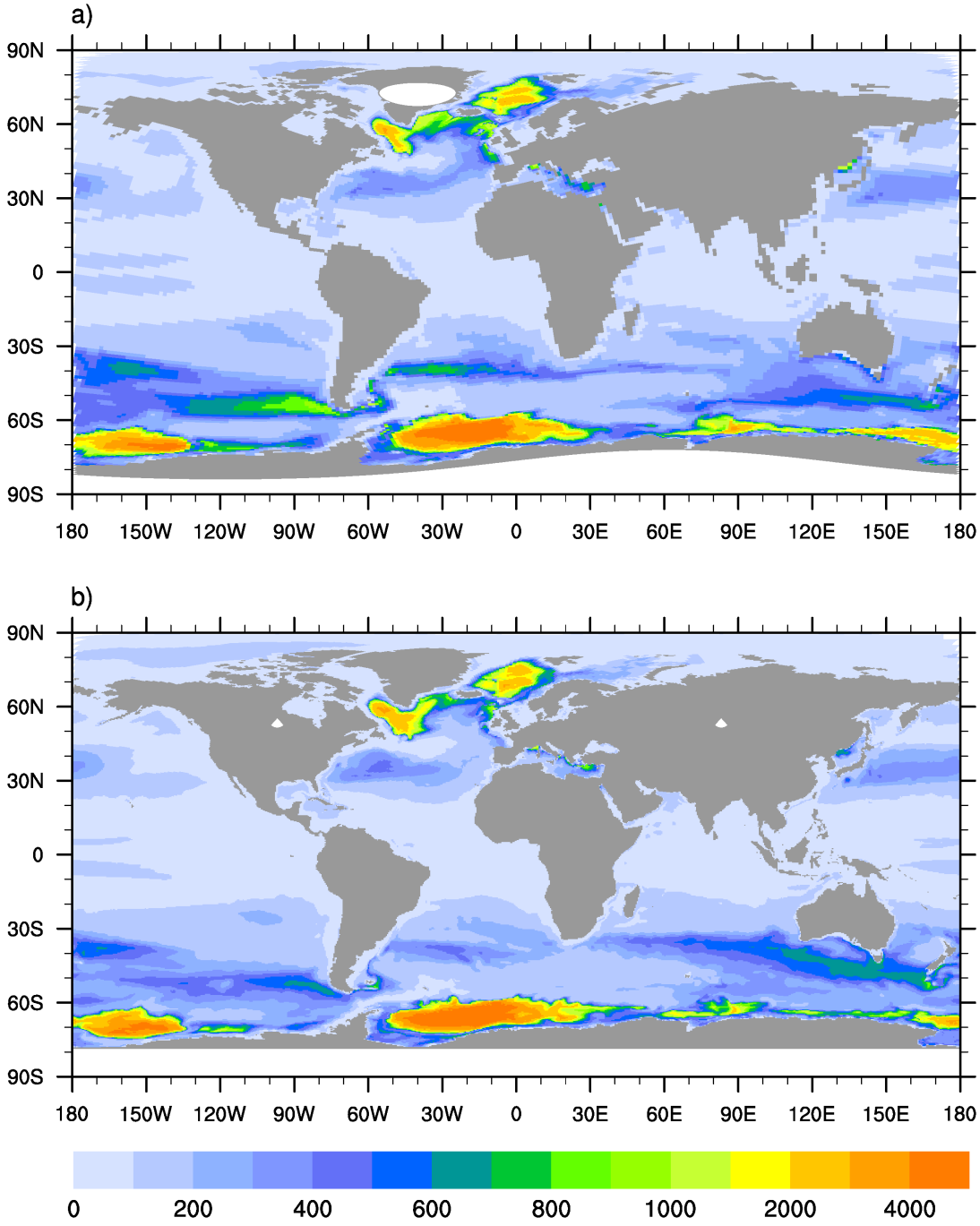

Figure 9. Yearly maximum MLD (m) from long-term monthly means from the PICTRL simulation for (a) MPI-ESM-LR, and (b) MPI-ESM-MR; the MLD is defined as the depth at which a 0.125 kg m^{-3} change of potential density with respect to the surface has occurred.

Table 3. Characteristics of the El Niño/Southern Oscillation in the HadISST Data, the CMIP3 Model System, and the Two MPI-ESM Versions Contributing to CMIP5

Amplitude	Niño4	Niño3.4	Niño3
Obs.	0.562	0.76	0.785
ECHAM5/MPIOM	1.13	1.26	1.21
MPI-ESM-LR	0.7	0.75	0.77
MPI-ESM-MR	0.59	0.76	0.67
Skewness			
Obs.	−0.15	0.4	0.77
ECHAM5/MPIOM	−0.28	0.08	0.20
MPI-ESM-LR	0.20	0.16	0.09
MPI-ESM-MR	0.06	0.03	−0.03

years. However, the more realistic representation of the ENSO power spectrum is found again in the LR configuration, which, in addition to the interannual variability, shows enhanced power at decadal time scale (Figure 10). This improvement compared to ECHAM5/MPIOM is most likely due to changes in the convection parameterization in ECHAM6 [*Stevens et al.*, 2013; *Guilyardi et al.*, 2012]. While the reduction in amplitude makes the MPI-ESM simulations superior to earlier model versions, this does not hold for other ENSO-related characteristics. The observed seasonal phase locking of ENSO to the boreal winter was better captured by the ECHAM5/MPIOM model, whereas the new model configurations show a weaker seasonal modulation of ENSO strength in addition to a secondary maximum of ENSO in late spring-early summer (not shown). The relative strength of El Niño versus La Niña events, or the "nonnormality of ENSO" [*Burgers and Stephenson*, 1999] is expressed in terms of a skewness parameter. For Niño3.4 and Niño3, the observational data (HadISST) [*Rayner et al.*, 2003] indicate a predominance of El Niño over the last 140 years. Compared to the observations and the CMIP3 model version, skewness indices are slightly degraded in the new model versions (Table 3), especially in the MR model that shows skewness close to zero. Determining the reason for this behavior is beyond the scope of this paper, but there are indications that this might be related to the modeled nonlinear response of the central Pacific zonal wind stress to SST anomalies [*Kang and Kug*, 2002; *Frauen and Dommenget*, 2010]. The spatial structure of ENSO is realistically simulated in both model versions (Figure 11). However, the more equatorially confined SST variability patterns stretch out further to the west compared to the observations. This spatial bias appears more pronounced in the LR configuration due to a too strong and too far westward extended equatorial cold tongue. Both model configurations simulate much weaker teleconnections towards the central subtropical North and South Pacific and tropical western Pacific than observed. The teleconnections to the Indian Ocean and Atlantic are reproduced relatively well and the weaker amplitude of the regression patterns in the Atlantic is another improvement over the ECHAM5/MPIOM model [cf., *Jungclaus et al.*, 2006, Figure 13].

5.2. Decadal to Multidecadal Variability in the Atlantic Circulation and Heat Transports

[49] Variations in the Atlantic MOC and, more importantly, the associated meridional heat transports are important drivers of low-frequency variations of North Atlantic SSTs [e.g., *Latif et al.*, 2004]. Moreover, oceanic variations on these time scales provide the long-term memory leading to skill in decadal predictions [*Matei et al.*, 2012]. The period and magnitude of MOC variations, as well as the underlying mechanisms, are highly model dependent [e.g., *Menary et al.*, 2012]. *Hurrell et al.* [2010] report pronounced differences in different versions of one model system, due to differences in resolution or in the parameterizations. The latter does not seem to be the case in MPI-ESM. Time-latitude plots of decadally smoothed total advective and overturning heat transport anomalies (Figure 12) display relatively similar characteristics. In both realizations, the magnitude of the anomalies is of the order of 0.1 PW, with somewhat higher amplitudes in LR. The decomposition into gyre and MOC components reveals that the latter is mainly responsible for the variations

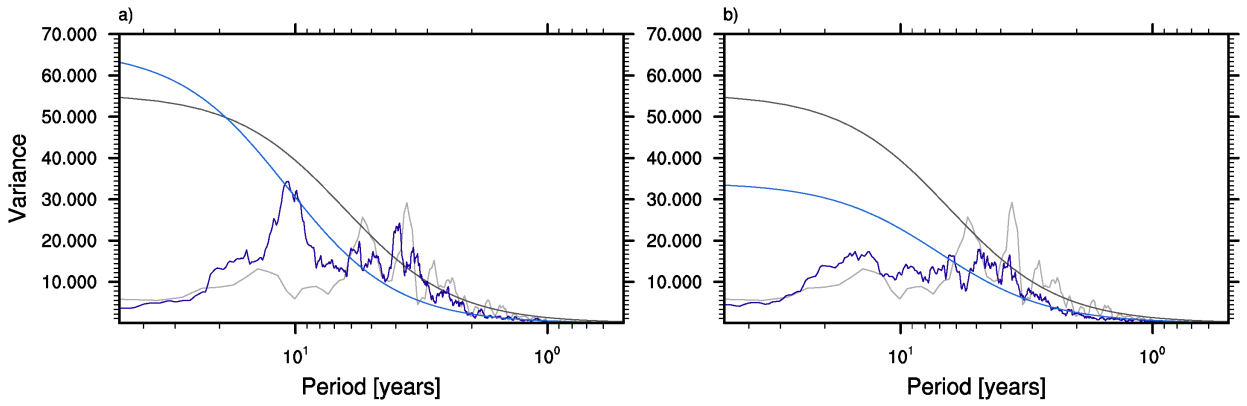

Figure 10. Variance spectra of monthly mean Niño3.4 SST anomalies (blue lines) from the PICTRL simulations obtained by (a) MPI-ESM-LR and (b) MPI-ESM-MR; grey lines indicate the respective spectrum from the HadISST data [*Rayner et al.*, 2003]; the smooth lines indicate the 95% significance level of a corresponding AR1 process.

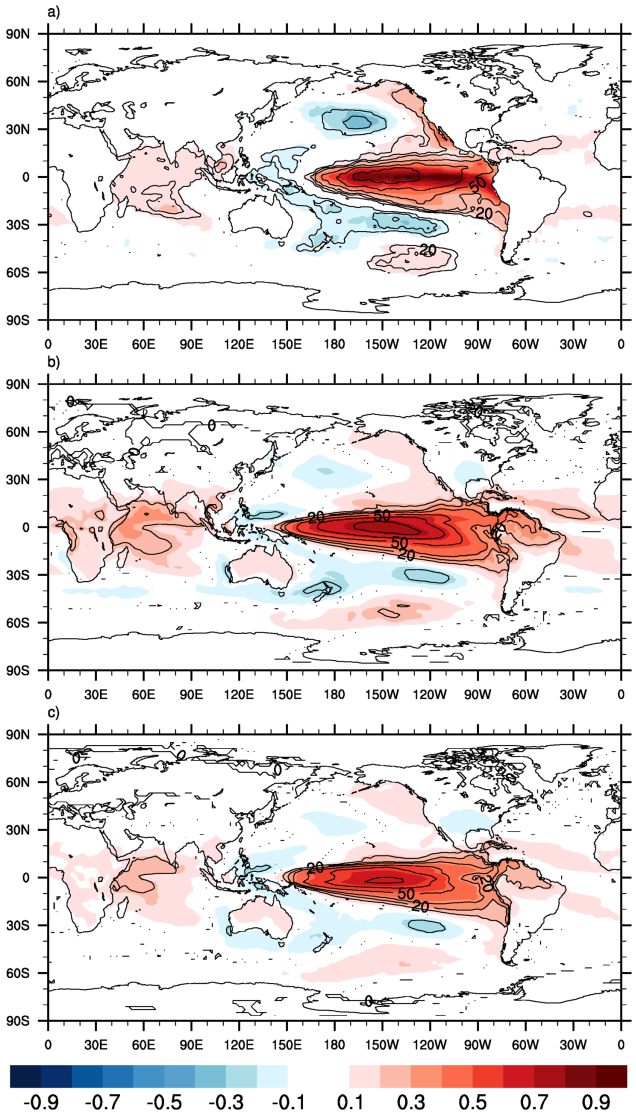

Figure 11. Regression (in K per standard deviation) of Niño3.4 temperature anomalies on global SST (shading), and explained variance (contours) for (a) the HadISST data, and the PICTRL simulations for (b) MPI-ESM-LR, and (c) MPI-ESM-MR. For the simulations also data for surface air temperatures over the continents are provided. Contour intervals for explained variance are 10%, 20%, 30%, 50%, 70%, and 90%.

south of 40°N, and the relative importance of both components changes roughly at the boundary between subtropical gyre and subpolar gyre. The variability regimes to the north and south of that boundary are also different. Spectra taken at 26.5°N and 48°N (not shown) exhibit peaks in variance between 30 and 50 years at the subpolar latitude and enhanced power at lower frequencies in the subtropics. Another, apparently resolution-dependent, aspect is that the overturning-related anomalies tend to migrate further to the north in LR. This is another consequence of the representation of the subpolar gyre that is probably too wide and stationary in MR. Details of the multidecadal variability in MOC and heat transport as well as the role of the gyre system in regulating the meridional heat transports are the subject of ongoing investigations and will be reported in an upcoming paper.

6. Ocean Model Resolution and Particular Circulation Patterns

[50] In this final section, we focus on two regions where the ocean resolution in the LR and MR configurations show fundamental differences. One region is the tropical Pacific ocean, the other the margin between the respective subtropical gyres and the ACC.

6.1. Equatorial Pacific

[51] Simulated currents and temperatures in the Pacific Ocean along the equator and at 110°W are compared with observations from *Johnson et al.* [2002] in Figure 13. The compilation of hydrographic observations and current measurements were obtained by an evaluation of several oceanographic sections from the 1990s. Along the Equator (Figure 13, left column), both model versions show a realistic representation of the position and slope of the 20°C isotherm, with a tighter thermocline in the MR simulation. In the observations, the 26°C isotherm outcrops near 140°W where isotherms in the simulations are closer to 24°C. The finer-resolution TP04 grid in MPI-ESM-MR delivers a clearly better representation of the core of the eastward flow along the thermocline, with more realistic speeds and location of the maximum. In comparison with the observations, the boundary between eastward and westward flow is, however, too shallow in MR whereas in LR, there is clearly too strong westward flow in the surface layers. At 110°W (Figure 13, right column), the TP04 grid allows for a good representation of the current system in terms of horizontal and vertical structure and amplitude. In particular, the position of the maximum and the tilt of the core of the equatorial undercurrent with depth are well captured. This holds also for the structure and the asymmetry of the south equatorial current system across the equator with highest speed near 2°N. Stratification in the upper layers appears to be stronger in the simulations, and both model versions are somewhat warmer than the observations below the thermocline. On the other hand, the observations only cover a limited period and may be subject to variability on various time scales.

6.2. Southern Ocean/South Atlantic transition

[52] Resolution-dependent differences between the LR and MR versions of MPI-ESM have shown up most clearly in the transition region between Southern Ocean and South Atlantic. Intermediate-depth temperature and salinity biases (Figure 3) indicate an overestimation of the input of warm and saline Indian Ocean waters, and the BSF (Figure 4) shows pronounced differences in the Agulhas region and the confluence zone along the Brazilian coast. This part of the world ocean has received increased attention in recent years because of its role in regulating the freshwater (salt) and heat

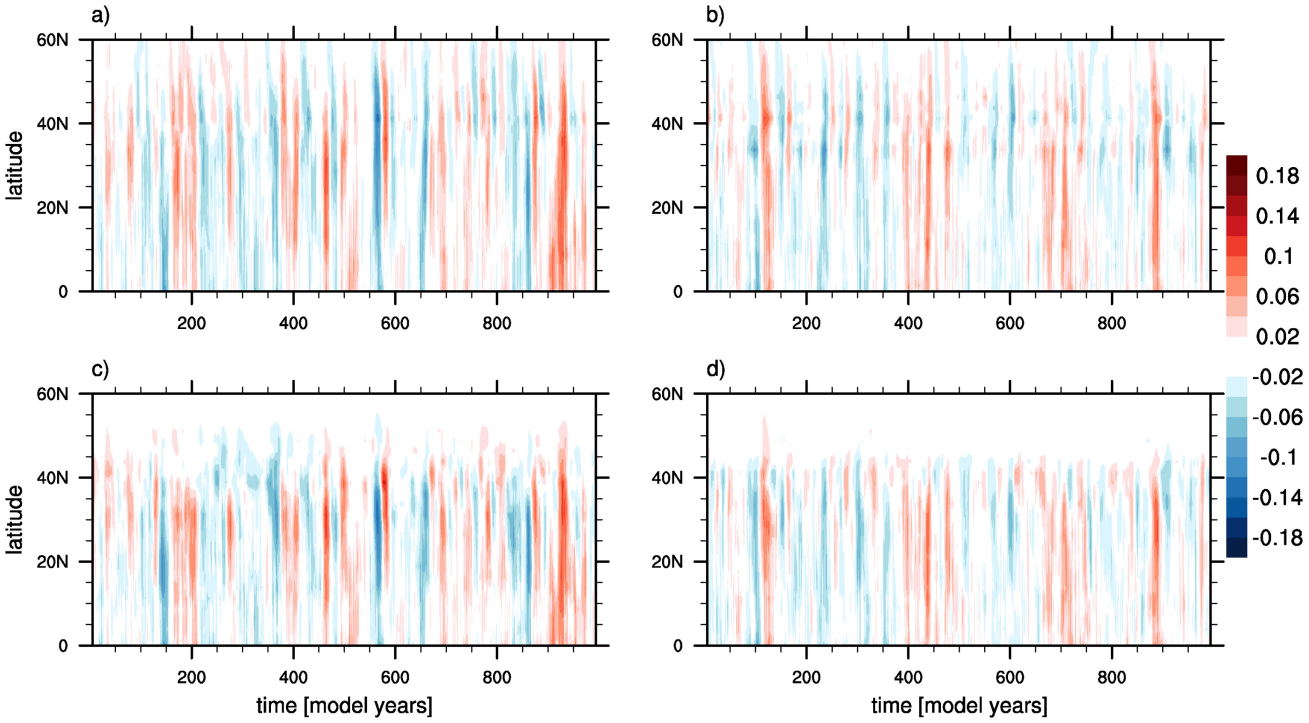

Figure 12. Ocean advective heat transport anomalies (PW) from the PICTRL simulations: (a, b) total heat transport, and (c, d) heat transport contribution from the meridional overturning circulation for (left) MPI-ESM-LR, and (right) MPI-ESM-MR. All data sets were smoothed using an 11 year running mean.

input into the Atlantic and possible consequences for the stability of the Atlantic MOC [*De Vries and Weber*, 2005; *Biastoch et al*., 2009; *Lee et al*., 2011]. The greater Agulhas system feeds the upper limb of the overturning circulation through the "leakage" of warm and salty waters from the Indian Ocean to the Atlantic [*Beal et al*., 2011]. Hydrographic observations demonstrate that the Agulhas current, after having passed the southern tip of Africa, turns south and then forms the so-called Agulhas retroflection, where the Agulhas current loops back into the Indian Ocean [*Lutjeharms and van Ballegooyen*, 1988]. The leakage is thought to be mainly maintained by the shedding of Agulhas rings, i.e., eddies carrying warm and salty waters. The system is prone to strong variations related to the dynamics of the current system and the position of the zero line of wind stress curl [*Beal et al*., 2011].

[53] Comparing in more detail the MPI-ESM LR and MR model solutions, it is clear that only the higher-resolution model allows for the formation of a pronounced retroflection pattern (Figure 14). In MR, the Agulhas current (AC) is simulated as a narrow boundary current that is retroflected back into the Indian Ocean forming the Agulhas return current (ARC), clearly to be identified in Figure 14b. The formation of anticyclonic eddies, resembling Agulhas rings, can also be seen in the MR realization. In the LR setup, the AC largely continues into the Atlantic and feeds a southern hemisphere "supergyre" [e.g., *Speich et al*., 2007]. The subtropical front south of Africa is situated more to the south in LR; in fact, the position of the zero line of the BSF along 20°E differs by about 4° latitude (Figure 14a). This feature is clearly related to a lack of resolution. A similar difference occurs in the uncoupled ocean simulations. This is not surprising as eddies play an important role for the dynamics of the ACC and the retroflection. The intensity of mesoscale activity is reflected in the variance of sea surface height (SSH). The standard deviations obtained from monthly SSH data from the respective simulations are compared with data derived from satellite altimetry (AVISO, http://aviso.oceanobs.com/duacs/) in Figure 15. The observational data identify the AC and ARC as narrow and meandering flows. The northwestward orientated tongue of high eddy activity in the Cape Basin indicates the shedding of Agulhas rings and their pathway into the South Atlantic. None of these features is captured by the LR model, although there is some enhanced variance to the south of Africa related to variations of the BSF. In contrast, although underestimating the magnitude of the variance in comparison with the observations, the MR realization includes the position and width of the ARC as well as the shape and orientation of the Agulhas rings' pathway. At eddy-permitting resolution, the MR model is clearly not able to reproduce all the details of mesoscale activity in the real Agulhas system. *Biastoch et al*. [2008] have demonstrated that for this purpose, eddy-resolving (0.1°) resolution is necessary and that eddy-permitting models tend to produce Agulhas rings too regularly. Nevertheless, the MR model includes, with its ability to simulate rings carrying Indian Ocean water masses into the Atlantic, a considerably improved

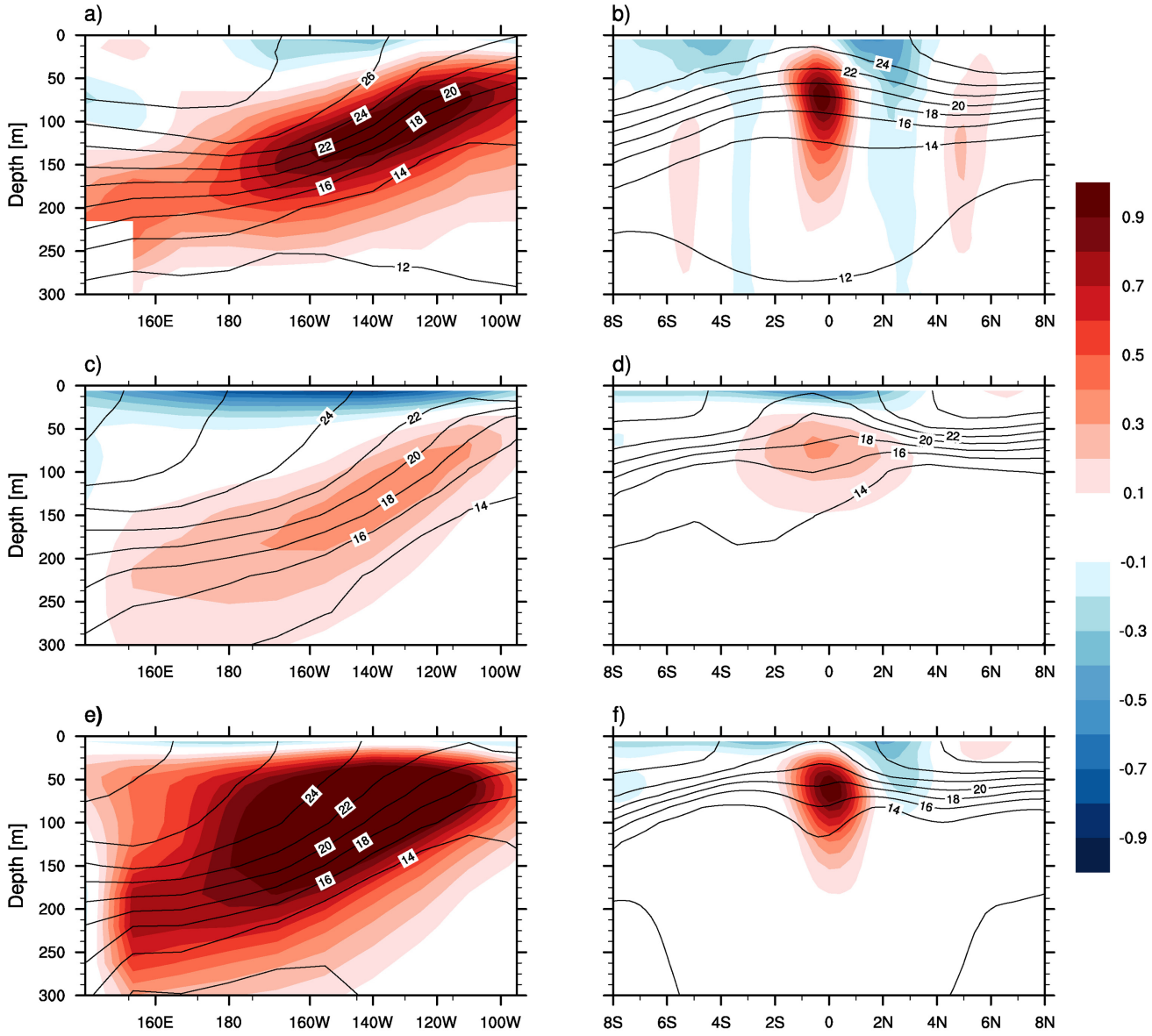

Figure 13. Zonal velocities (shading) and temperatures (contours) in the Pacific Ocean (left column) along the Equator, and (right column) at 110°W from long-term means of the PICTRL simulations: (middle row) MPI-ESM-LR, and (bottom row) MPI-ESM-MR; the top row shows observational data from *Johnson et al.* [2002].

representation of the exchange of mass, heat, and salt at this key location of the thermohaline circulation.

[54] In contrast to the MR simulation, the Agulhas current in the LR setup continues into the South Atlantic subtropical gyre, and the opening between the two oceans, as defined by the zero line of the BSF, is much broader. The differences in circulation seen at the surface carry on in the deeper layers (not shown), and the intermediate depth flow carries overly warm and salty water into the Atlantic, where it accumulates in the subtropical gyre. These water-mass differences also contribute to the much stronger South Atlantic subtropical gyre in LR.

[55] The differences in the hydrography and circulation also have consequences for the heat and freshwater transport into the South Atlantic. *De Vries and Weber* [2005], by applying a freshwater flux anomaly, have demonstrated that modification of the salinity properties can lead to pronounced changes in the relative contribution of gyre and overturning component of the meridional freshwater transports, and this is what we diagnose in our analysis. Figure 6d demonstrates that both configurations simulate a similar (about 0.2 Sv) total freshwater transport at 34°S, but with different contributions from the subcomponents. While the overturning contribution is near zero in LR, it is clearly negative (−0.14 Sv) in MR. Given that the MR model simulates the South Atlantic circulation and hydrography more realistically than the LR model, it seems reasonable to also assume that the sign of the freshwater transport is better reproduced in the higher-resolution model. The notion of a freshwater exporting overturning

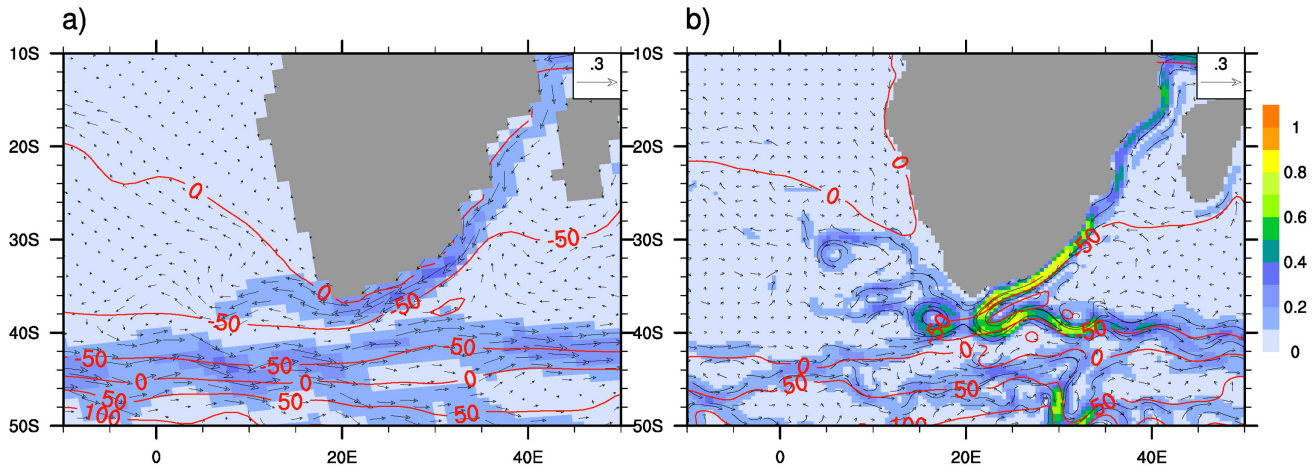

Figure 14. Snapshots of the velocity fields in the Agulhas region displayed as vectors and absolute velocity ($m\,s^{-1}$, shading) obtained from monthly mean data; red contour lines indicate the long-time means of the BSFs (Sv) from the PICTRL simulations: (a) MPI-ESM-LR and (b) MPI-ESM-MR.

circulation is also supported by recent evaluations of observations [*Huisman et al.*, 2010; *Bryden et al.*, 2011] and ocean reanalyses [*Hawkins et al.*, 2011]. In contrast, most CMIP3 models show freshwater import by the overturning component [*Drijfhout et al.*, 2010].

[56] Earlier studies have suggested that the sign of the overturning component can be used as an indicator for MOC stability such that the Atlantic MOC is bistable if it imports its own salt [*Rahmstorf*, 1996; *Dijkstra*, 2007; *Hawkins et al.*, 2011]. At present, we do not have freshwater perturbation experiments at hand for the model configurations discussed here. A preliminary evaluation of the CMIP5 idealized global warming experiments in the two model configurations indicate a stronger decrease of the Atlantic heat transport in the MR simulation by the time the simulations reach four times preindustrial CO_2. However, the experiments were not carried out long enough to assess any MOC recovery behavior, and the experimental setup does not allow for a clear discrimination between oceanic and atmospheric processes, or if the stronger decline in MR just follows from the different mean state in the unperturbed run. In the near future, water hosing experiments [*Stouffer et al.*, 2006; *Swingedouw et al.*, 2012] will be carried out to study, in detail, the stability of the MOC in the two model setups.

7. Summary and Conclusion

[57] This paper provides a description of MPIOM as the ocean component of the MPI-ESM. A basic evaluation based on long control simulations and ensembles of historical integrations is presented for two model configurations: MPI-ESM-LR and MPI-ESM-MR. The two setups differ in the vertical resolution in the atmosphere and the horizontal resolution in the ocean.

[58] Compared to the CMIP3 model system ECHAM5/MPIOM [*Jungclaus et al.*, 2006], we have diagnosed improvements mainly regarding features that are related to changes in the atmosphere model. This comes as no surprise as the ocean model did not change apart from technical developments and the CMIP3 model also applied the same ocean grid as MPI-ESM-LR. *Stevens et al.* [2013] have documented the development steps leading from ECHAM5 to ECHAM6 analyzing atmosphere stand-alone simulations. They conclude that higher vertical resolution in the middle atmosphere lead to improvements in the extratropical circulation, a better representation of the middle atmosphere, and a systematic reduction of temperature biases in the upper troposphere. For the coupled system and the ocean, improvements can be seen most notably in the ENSO amplitude and in the circulation over the Arctic. The latter is likely related to an improved representation of parameterized gravity waves (Mauritsen, personal communication). In the analysis provided here, we have focused on the mean state and main variability features and we have not found many differences that could be related to the further increased vertical resolution in the MR atmosphere (95 versus 47 levels). Further research will study details of stratosphere-troposphere interaction and their role for coupled ocean-atmosphere processes [e.g., *Manzini et al.*, 2012] in more detail.

[59] Comparing the surface properties of the MR and LR simulations reveals that applying higher resolution leads to an improvement in the North Pacific, the eastern tropical Pacific, the southern South Atlantic and southern Indian Ocean, whereas the North Atlantic and the Labrador Sea are less well simulated in MPI-ESM-MR. The two ocean model grids (GR1.5 and TP0.4) discussed here differ not only in their nominal resolution but also in the placements of the poles of the curvilinear grids. While TP04 features quasi-homogeneous resolution over the ocean (because the northern grid poles are placed over large Northern Hemisphere land masses), the northern pole in GR1.5 is located over Greenland. The resulting resolution convergence can be seen as an advantage because it allows for a relatively good representation of the deepwater formation centers

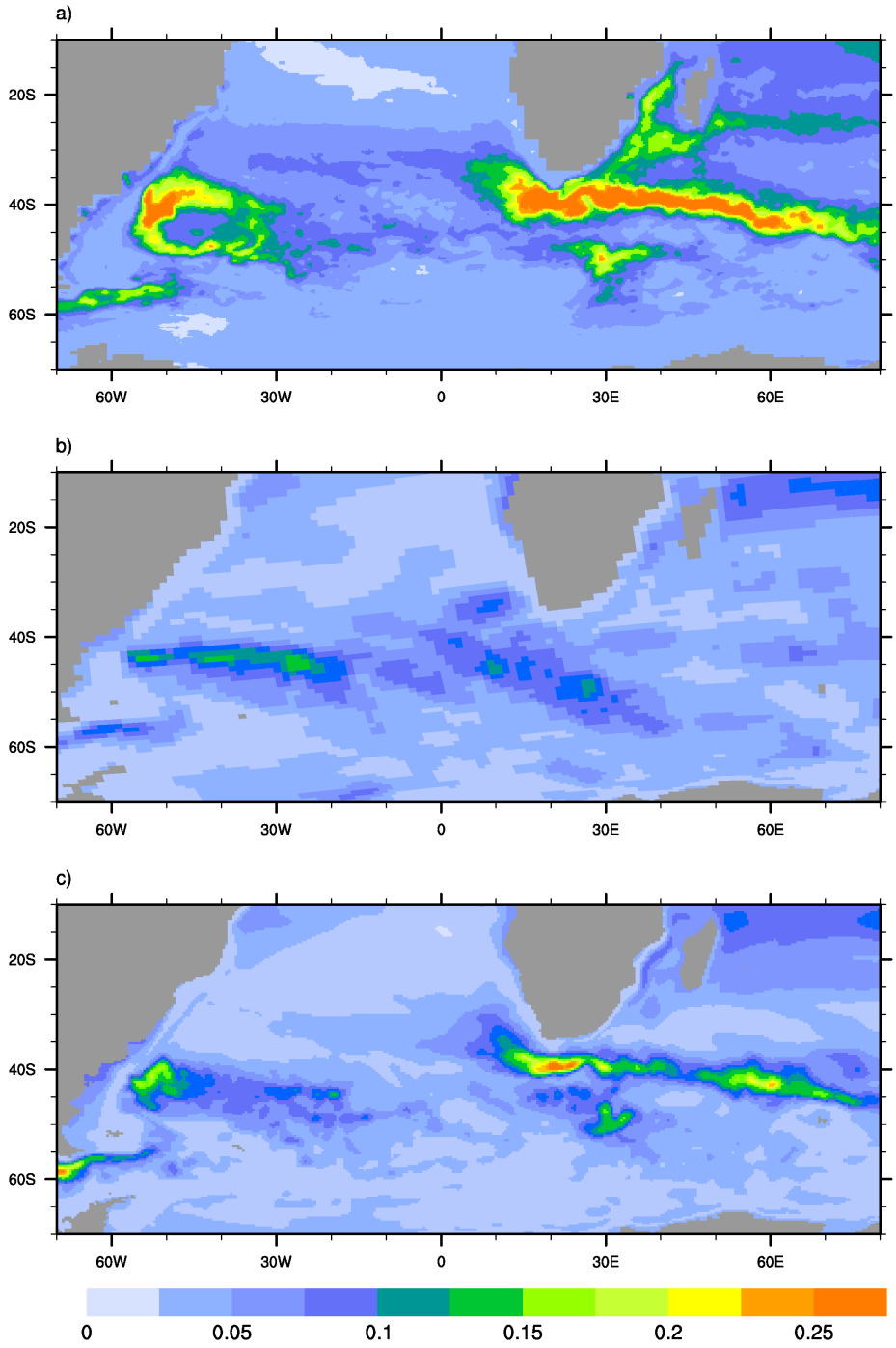

Figure 15. Sea surface height standard deviation (m) from monthly mean data for (a) satellite-based observations (AVISO), and for the PICTRL simulations: (b) MPI-ESM-LR and (c) MPI-ESM-MR.

in the Labrador Seas and in the Nordic Seas and in the overflow channels across the GSR. Thus, while resolution-dependent improvements can be clearly seen in the TP04 model in the tropical circulation and in the South Atlantic, a less good performance in the North Atlantic and in terms of overflow water masses could be a consequence of a better representation of these regions in the GR1.5 grid. However, since a much higher resolution of the GR class grid does not appear appropriate we expect further convergence at eddy-resolving resolution in a coupled model with a TP6M grid.

[60] Many of the biases with respect to observational estimates occurred also in the earlier version ECHAM5/MPIOM indicating a need for further model improvement in the coupled system. This holds, in particular, for the warm biases in the upwelling regions along the west coasts of North and South America and southern Africa, and the cold bias along the equator in the

Pacific. The cold bias in the North Atlantic, however, seems to be predominantly a problem of the ocean model. Recent progress has been documented by *Bryan et al*. [2007] and *Danabasoglu et al*. [2012], arguing for a better representation of the overflows and, eventually, for eddy-resolving resolution in global models.

[61] Subsurface quantities also show resolution-dependent differences. Most notably, the errors in intermediate-depth water mass properties in the South Atlantic, which appear most pronounced in the LR configuration, are related to the overestimation of heat and salt transfer from the Indian Ocean into the South Atlantic. At eddy-permitting resolution, the MR configuration provides a much better representation of the Agulhas current system, and such local mesoscale dynamics turn out to be an important ingredient for a proper representation of the mean state in the Atlantic.

[62] While the resolution-dependent differences between the LR and MR configurations give insight into important aspects of the underlying dynamics, it is also worth noting that the MPI-ESM setups behave rather similarly in many aspects. In particular, the control experiment variability characteristics, as described here in terms of ENSO and Atlantic heat transport variability, appear to be quite robust in terms of amplitude and spectrum.

[63] Ocean-only experiments indicate that the "eddy-permitting" model configuration may have to be just an intermediate step toward a globally eddy-resolving ocean component in an ESM. For example, *Farneti and Delworth* [2010] show a resolution-dependent response of the MOC to southern hemisphere wind changes, and *Biastoch et al*. [2008] have demonstrated that an eddy-resolving resolution of 0.1° is necessary to adequately simulate the shedding of Agulhas rings. This is also what we find in ocean-only simulations with the MPIOM TP6M setup at globally 0.1° resolution (von Storch, submitted), but the computational costs of such a system prevent us from running such a model coupled to a high-resolution atmosphere. On the other hand, regional grid refinement, for example in the overflow region or the Agulhas region, might be another strategy. At MPI-M, model development will explore directions as well as new dynamical cores and further improvements in the representation of oceanic processes.

[64] **Acknowledgments.** The authors thank the scientific programmers at MPI-M and the staff of the German Climate Computing Center (DKRZ) for their support in developing the model and conducting the model experiments. The CMIP5 simulations have been funded by the Federal Ministry for Education and Research in Germany (BMBF). J.H.J. acknowledges funding through the BMBF research program "MiKlip" (FKZ: 01LP1158A), and D.M. received financial support through the BMBF research program "Nordatlantik" (FKZ: 03F0605D/E). K.L. was supported through the Cluster of Excellence "CLISAP" at Hamburg University, funded by the German Science Foundation (DFG). We thank Achim Stössel, Stephen Griffies, and one anonymous reviewer for comments and suggestions that helped to improve the manuscript.

References

Antonov, J. I., D. Seidov, T. P. Boyer, R. A. Locarnini, A. V. Mishonov, H. E. Garcia, O. K. Baranova, M. M. Zweng, and D. R. Johnson (2010), *World Ocean Atlas 2009*, vol. *2*, Salinity, NOAA Atlas NESDIS 69, edited by S. Levitus, 184 pp., U.S. Gov. Print. Off., Washington, D.C.

Biastoch, A., J. R. E. Lutjeharms, C. W. Böning, and M. Scheinert (2008), Mesoscale perturbations control inter-ocean exchange south of Africa, *Geophys. Res. Lett.*, *35*, L20602, doi:10.1029/2008GL35132.

Biastoch, A., C. W. Böning, F. U. Schwarzkopf, and J. R. E. Lutjeharms (2009), Increase in Agulhas leakage due to poleward shift of Southern Hemisphere westerlies, *Nature*, *462*, 495–499, doi:10.1038/nature/08519.

Beal, L-M., W. P. M. De Ruijter, A. Biastoch, R. Zahn, and SCOR/WCRP/IAPSO Working Group 136 (2011), On the role of the Agulhas system in ocean circulation and climate, *Nature*, *472*, 429–436, doi:10.1038/nature09983.

Braconnot, P., S. P. Harrison, M. Kageyama, P. J. Bartlein, V. Masson-Delmotte, A. Abe-Ouchi, B. Otto-Bliesner, and Y. Zhao (2012), Evaluation of climate models using paleoclimatic data, *Nat. Clim. Change*, *2*, 417–424, doi:10.1038/nclimate1456.

Brovkin, V., L. Boysen, T. Raddatz, V. Gayler, A. Loew, and M. Claussen (2013), Evaluation of vegetation cover and land-surface albedo in MPI-ESM CMIP5 simulations, *J. Adv. Model. Earth Syst.*, *5*, doi:10.1029/2012MS000169.

Bryan, F. O., M. W. Hecht, and R. D. Smith (2007), Resolution convergence and sensitivity studies with North Atlantic circulation models. Part I: The western boundary current system, *Ocean Modell.*, *16*, 141–159, doi:10.1016/j.ocemod.2006.08.005.

Bryden, H. L., A. B. King, and G. D. McCarthy (2011), South Atlantic overturning circulation at 24°S, *J. Mar. Res.*, *69*(1), 38–55.

Burgers, G., and D. B. Stephenson (1999), The "normality" of El Niño, *Geophys. Res. Lett.*, *26*, 1027–1030.

Carton, J. A., and B. S. Giese (2008), A reanalysis of ocean climate using simple ocean data assimilation (SODA), *Mon. Weather Rev.*, *136*, 2999–3017, doi:10.1175/2007MWR1978.1.

Clarke, R. A. (1984), Transport through the Cape Farewell-Flemish Cap section, *Rapp. P. V. Reun. Cons. Int. Explor. Mer.*, *185*, 120–130.

Cunningham, S. A., S. G. Alderson, B. A. King, and M. A. Brandon (2003), Transport and variability of the Antarctic circumpolar current in Drake Passage, *J. Geophys. Res.*, *108*(C5), 8084, doi:10.1029/2001JC001147.

Danabasoglu, G., W. G. Large, and B. P. Briegleb (2010), Climate impacts of parameterized Nordic Seas overflows. *J. Geophys. Res.*, *115*, C11005, doi:10.1029/2010JC006243.

Danabasoglu, G., S. C. Bates, B. P. Briegleb, S. R. Jayne, M. Jochum, W. G. Large, S. Peacock, and S. G. Yeager (2012), The CCSM4 ocean component, *J. Clim.*, *25*, 1361–1389, doi:10.1175/JCLI-D-11–00091.1.

Delworth, T. L., et al. (2012), Simulated climate and climate change in the GFDL CM2.5 high-resolution coupled climate model, *J. Clim.*, *25*, 2755–2781, doi:10.1175/JCLI-D-11–00316.1.

Dengg, J., A. Beckmann, and R. Gerdes (1996), The Gulf Stream separation problem, in *The Warmwatersphere of the North Atlantic Ocean*, edited by W. Krauss, pp. 253–290, Gebr. Bornträger, Berlin.

De Vries, P., and S. L. Weber (2005), The Atlantic freshwater budget as a diagnostic for the existence of a stable shut down of the meridional overturning circulation, *Geophys. Res. Lett.*, *32*, L09606, doi:10.1029/2004GL021450.

Dickson, R. R., and J. Brown (1994), The production of North Atlantic Deep Water: Sources, rates, and pathways, *J. Geophys. Res.*, *99*, 12,319–12,341.

Dijkstra, H. A. (2007), Characterization of the multiple equilibria regime in a global ocean model, *Tellus Ser. A*, *59*, 695–705, doi:10.1111/j.1600-0870.2007.00267x.

DiMarco, S. F., P. Chapman, W. D. Nowlin Jr., P. Hacker, K. Donohue, M. Luther, G. C. Johnson, and J. Toole (2002), Volume transport and property distribution of the Mozambique Channel, *Deep-Sea Res. II*, *49*, 1481–1511.

Drijfhout, S. S., S. L. Weber, and E. van der Swaluw (2010), The stability of the MOC as diagnosed from model projections for the pre-industrial, present, and future climates, *Clim. Dyn.*, *37*, 1575–1586.

Farneti, R., and T. L. Delworth (2010), The role of mesoscale eddies in the remote response to altered Southern Hemisphere winds, *J. Phys. Oceanogr.*, *40*, 2348–2354, doi:10.1175/2010JPO4480.1.

Fasullo, J. T., and K. E. Trenberth (2008), The annual cycle of the energy budget. Part II: Meridional structure and poleward transports, *J. Clim.*, *21*, 2313–2325.

Frauen, C., and D. Dommenget (2010), El Nino and La Nina amplitude asymmetry caused by atmospheric feedbacks, *Geophys. Res. Lett.*, *37*, L18801, doi:10.1029/2010GL044444.

Friedlingstein, P., et al. (2006), Climate-carbon cycle feedback analysis: Results from the C4MIP model intercomparison, *J. Clim.*, *19*, 3337–3353.

Ganachaud, A., and C. Wunsch (2003), Large-scale ocean heat and fresh water transports during the World Ocean Circulation experiment, *J. Clim.*, *16*, 696–705.

Gent, P. R., J. Willebrand, T. McDougall, and J. C. McWilliams (1995), Parameterizing eddy-induced tracer transports in ocean circulation models, *J. Phys. Ocenogr.*, *25*, 463–474.

Gent, P. R., W. G. Large, and F. O. Bryan (2001), What sets the mean transport through Drake Passage? *J. Geophys. Res.*, *106*, 2693–2712.

Gerdes, R., and C. Köberle (1995), Influence of DSOW on the North Atlantic general circulation, *J. Phys. Oceanogr.*, *25*, 2624–2642.

Gordon, A. L. (1978), Deep Antarctic convection west of Maud Rise, *J. Phys. Oceanogr.*, *8*, 600–612.

Gordon, A. L. (1986), Inter-ocean exchange of thermocline water, *J. Geophys. Res.*, *91*, 5037–5046.

Gordon, A. L., J. Sprintall, H. M. Van Aken, D. Susanto, S. Wijffels, R. Molcard, A. Ffield, W. Pranowo, and S. Wirasantosa (2010), The Indonesian throughflow during 2004–2006 as observed by the INSTANT program, *Dyn. Atmos. Oceans*, *50*, 115–128, doi:10.1016/j.dynatnoce.2009.12.002.

Griffies, S. M., R. C. Pacanowski, and R. W. Hallberg (2000), Spurious diapycnal mixing associated with advection in a z-coordinate ocean model, *Mon. Weather Rev.*, *128*, 538–564.

Griffies, S. M., et al. (2009), Coordinated ocean-ice reference experiments (COREs), *Ocean Modell.*, *26*, 1–46, doi:10.1016/j.ocemod.2008.08.007.

Griffies, S. M., et al. (2011), The GFDL CM3 coupled climate model: Characteristics of the ocean and sea-ice simulations. *J. Clim.*, *24*, 3520–3544, doi:10.1175/2011JCLI3964.1.

Grodsky, S. A., J. A. Carton, S. Nigam, and Y. M. Okumura (2012), Tropical Atlantic biases in CCSM4, *J. Clim.*, *25*, 3684–3701, doi:10.1175/JCLI-D-11–00315.1.

Guilyardi, E., H. Bellenger, M. Collins, S. Ferrett, W. Cai, and A. Wittenberg (2012), A first look at ENSO in CMIP5, *CLIVAR Exch.*, *58*, 29–32.

Haak, H., J. H. Jungclaus, U. Mikolajewicz, and M. Latif (2003), Formation and propagation of great salinity anomalies, *Geophys. Res. Lett.*, *30*(9), 1473, doi:10.1029/2003GL017065.

Hagemann, S., and L. Dümenil-Gates (2003), An improved sub grid runoff parameterization scheme for climate models, *Clim. Dyn.*, *21*, 349–359.

Hagemann, S., A. Loew, and A. Andersson (2013), Combined evaluation of MPI-ESM land surface water and energy fluxes, *J. Adv. Model. Earth Syst.*, doi:10.1029/2012MS000173, in press.

Hansen, B., and S. Østerhus (2007), Faroe bank channel overflow 1995–2001, *Prog. Oceanogr.*, *75*, 817–856, doi:10.1016/j.pocean.2007.09.004.

Hansen, B., S. Østerhus, W. R. Turrell, S. Jónsson, H. Valdiarsson, H. Hátún, and S. M. Olsen (2008), The inflow of Atlantic water, heat, and salt to the Nordic Seas across the Greenland-Scotland Ridge, in *Arctic-Subarctic Ocean Fluxes*, edited by R. R. Dickson et al., pp. 15–43, Springer, Dordrecht, Netherlands.

Hawkins, E., R. S. Smith, L. C. Allison, J. M. Gregory, T. J. Woolings, H. Pohlmann, and B. de Cuevas (2011), Bistability of the Atlantic overturning circulation in a global climate model and links to freshwater transport, *Geophys. Res. Lett.*, *38*, L10605, doi:10.1029/2011GL047208.

Hibler, W. D., III (1979), A dynamic thermodynamic sea ice model, *J. Phys. Oceanogr.*, *9*, 815–846.

Huisman, S. E., M. den Toom, H. A. Dijkstra, and S. Drijfhout (2010) An indicator of the multiple equilibria regime of the Atlantic meridional overturning circulation, *J. Phys. Oceanogr.*, *40*, 551–567, doi:10.1175/2009JPO4215.1.

Hurrell, J. W., et al. (2010), Decadal climate prediction: Opportunities and challenges, in *Proceedings of OceanObs09: Sustained Ocean Observations and Information for Society, vol. 2*, edited by J. Hall, D. E. Harrison, and D. Stammer, ESA Publ. WPP-306, doi:10.5270/OceanObs.cwp45.

Ilyina, T., K. D. Six, J. Segschneider, E. Maier-Reimer, H. Li, and I. Núñez-Riboni (2013), The global ocean biogeochemistry model HAMOCC: Model architecture and performance as component of the MPI-Earth System Model in different CMIP5 experimental realizations, *J. Adv. Model. Earth Syst.*, doi:10.002/jame.20017.

Imawaki, S., H. Uchida, H. Ichikawa, M. Fukasawa, S. Umatani, and the ASUKA Group (2001), Satellite altimeter monitoring of the Kuroshio transport south of Japan. *Geophys. Res. Lett.*, *28*, 17–20.

Jayne, S. R., et al. (2009), The Kuroshio extension and its recirculation gyres, *Deep-Sea Res. I*, *56*, 2088–2099.

Johns, W., T. Shay, J. Bane, and D. Watts (1995), Gulf Stream structure, transport, and recirculation near 68°W, *J. Geophys. Res.*, *100*, 817–838.

Johns, W. E. et al. (2011), Continuous, array-based estimates of Atlantic Ocean heat transports at 26.5°N, *J. Clim.*, *24*, 2429–2449.

Johnson, G. C., B. M. Sloyan, W. S. Kessler, and K. E. McTaggert (2002), Direct measurements of upper ocean currents and water properties across the tropical Pacific during the 1990s, *Prog. Oceanogr.*, *52*, 31–61.

Jungclaus, J. H., N. Keenlyside, M. Botzet, H. Haak, J.-J. Luo, M. Latif, J. Marotzke, U. Mikolajewicz, and E. Roeckner (2006), Ocean circulation and tropical variability in the coupled model ECHAM5/MPI-OM, *J. Clim.*, *19*, 3952–3972.

Jungclaus, J. H., A. Macrander, and R. H. Käse (2008), Modelling the overflow across the Greenland-Scotland Ridge, in *Arctic-Subarctic Ocean Fluxes*, edited by R. R. Dickson et al., pp. 527–549, Springer, Dordrecht, Netherlands.

Jungclaus, J. H., et al. (2010), Climate and carbon-cycle variability over the last millennium, *Clim. Past.*, *6*, 723–737, doi:10.5194/cp-6–723-2010.

Kalnay, E., et al. (1996), The NCEP/NCAR 40-year reanalysis project, *Bull. Am. Meteorol. Soc.*, *77*, 437–471.

Kang, I. S., and J. S. Kug (2002), El Nino and La Nina sea surface temperature anomalies: Asymmetry characteristics associated with their wind stress anomalies, *J Geophys. Res.*, *107*(D19), doi:10.1029/2001JD000393.

Kanzow, T., et al. (2010), Seasonal variability of the Atlantic meridional overturning circulation at 26.5°N, *J. Clim.*, *23*, 5678–5698, doi:10.1175/2010JCLI3389.1.

Kara, A. B., P. A. Rochford, and H. E. Hurlburt (2003), Mixed layer depth variability over the global ocean, *J. Geophys. Res.*, *108*(C3), 3079, doi:10.1029/2000JC00736.

Koldunov, N. Y., D. Stammer, and J. Marotzke (2010), Present-day Arctic sea ice variability in the coupled ECHAM5/MPI-OM model, *J. Clim.*, *23*, 2520–2543, doi:10.1175/JCLI3065.1.

Large, W. G., and G. Danabasoglu (2006), Attribution and Impacts of Upper-Ocean Biases in CCSM3, *J. Climate*, *19*, 2325–2346, doi:http://dx.doi.org/10.1175/JCLI3740.1.

Latif, M., M. Botzet, M. Esch, H. Haak, S. Hagemann, J. H. Jungclaus, S. Legutke, S. Marsland, U. Mikolajewicz, and J. Mitchell (2004), Reconstructing, monitoring, and predicting decadal-scale changes in the North Atlantic thermohaline circulation with sea surface temperature, *J. Clim.*, *17*, 1605–1614.

Lee, S.-K., W. Park, E. van Sebille, M. O. Baringer, C. Wang, D. B. Enfield, S. G. Yeager, and B. P. Kirtman (2011), What caused the significant increase in Atlantic Ocean heat content since the mid-20th century? *Geophys. Res. Lett.*, *38*, L17607, doi:10.1029/2011GL048856.

Levitus, S., T. P. Boyer, M. E. Conkright, D. Johnson, T. O'Brien, J. Antonov, C. Stephens, and R. Gelfield (1998), NOAA Atlas NESDIS 19,World Ocean Database 1998 Volume 2: Temporal Distribution of Mechanical Bathythermograph Profiles, U.S. Gov. Printing Office, Wash., D.C., 286 pp.

Lindsay, R. W., and J. Zhang (2006), Assimilation of sea ice concentration in an ice-ocean model, *J. Atmos. Ocean. Technol.*, *23*, 742–749, doi:10.1175/JTECH1871.1.

Lutjeharms, J. R. E., and R. C. Van Ballegooyen (1988), The retroflection of the Agulhas current, *J. Phys. Oceanogr.*, *18*, 1570–1583.

Macrander, A., U. Send, H. Valdimarsson, S. Jónsson, and R. H. Käse (2005), Interannual changes in the overflow from the Nordic Seas into the Atlantic Ocean through Denmark Strait, *Geophys. Res. Lett.*, *32*, L06606, doi:10.1029/2004GL021463.

Maier-Reimer, E. (1997), Design of a closed boundary regional model of the Arctic Ocean, paper presented at Workshop on Polar Processes in Global Climate, *Bull. Amer. Meteor. Soc.*, 13–15 Nov. 1996.

Manzini, E., C. Cagnazzo, P. G. Fogli, A. Bellucci, and W. A. Müller (2012), Stratosphere–troposphere coupling at inter-decadal time scales: Implications for the North Atlantic Ocean, *Geophys. Res. Lett.*, *39*, L05801, doi:10.1029/2011GL05771.

Marsland, S. J., H. Haak, J. H. Jungclaus, M. Latif, and F. Röske (2003), The Max Planck Institute global ocean/sea ice model with orthogonal curvilinear coordinates, *Ocean Modell.*, *5*, 91–127.

Marsland, S. J., N. L. Bindoff, G. D. Williams, and W. F. Budd (2004), Modeling water mass formation in the Mertz Glacier Polynia and Adelie Depression, East Antarctic, *J. Geophys. Res.*, *109*, C11003, doi:10.1029/2004JC002441.

Mauritsen, T., et al. (2012), Tuning the climate of a global model, *J. Adv. Model. Earth Syst.*, *4*, M00A01, doi:10.1029/2012MS 000154.

Matei, D., J. Baehr, J. H. Jungclaus, H. Helmuth, W. A. Müller, and J. Marotzke (2012), Multiyear prediction of monthly-mean Atlantic meridional overturning circulation at 26.5°N. *Science*, *355*, 76–79, doi:10.1126/science.1210299.

Meier, W., F. Fetterer, M. Savoie, S. Mallory, R. Duerr, and J. Stroeve (2011), *NOAA/NSIDC climate data record of passive sea-ice concentration, Digital media*, National Snow and Ice Data Center, Boulder, Colo.

Menary, M., W. Park, K. Lohmann, M. Vellinga, M. D. Palmer, M. Latif, and J. H. Jungclaus (2012), A multimodel comparison of centennial Atlantic meridional overturning circulation variability, *Clim. Dyn.*, *38*, 2377–2388, doi:10.1007/s00382-011-1172-4.

Mikolajewicz, U., M. Vizcaino, J. H. Jungclaus, and G. Schurgers (2007), Moderate effect of interactive ice sheets in anthropogenic climate change simulations, *Geophys. Res. Lett.*, *34*, L18706, doi:10.10 29/2007GL031173.

Murray, R. J. (1996), Explicit generation of orthogonal grids for ocean models. *J. Comput. Phys.*, *126*, 251–273.

Notz, D., F. A. Haumann, H. Haak, J. H. Jungclaus, and J. Marotzke (2013), Arctic sea-ice evolution as modelled by MPI-ESM, *J. Adv. Model. Earth Syst.*, doi:10.1002/jame.20016, in press.

Nowlin Jr., W. D., and J. M. Klinck (1986), The physics of the Antarctic Circumpolar Current, *Rev. Geophys.*, *24*(3), 469–491, doi:10.1029/ RG024i003p00469.

Pacanowski, R. C., and S. G. H. Philander (1981), Parameterization of vertical mixing in numerical models of tropical oceans, *J. Phys. Oceanogr.*, *11*, 1443–1451.

Peterson, R., and L. Stramma (1991), Upper-level circulation in the South Atlantic Ocean, *Progr. Oceanogr.*, *26*, 1–73.

Pickart, R. S., D. T. Torres, and R. D. Clarke (2002), Hydrography of the Labrador Sea during active convection, *J. Phys. Oceanogr.*, *32*, 428–457.

Price, J. F., and M. O. Baringer (1994), Outflow and deep water production by marginal seas, *Progr. Oceanogr.*, *33*, 161–200.

Rahmstorf, S. (1996), On the fresh water forcing and transport of the Atlantic thermohaline circulation, *Clim. Dyn.*, *12*, 799–811.

Randall, D. A., R. A. Wood, S. Bony, R. Colman, T. Fichefet, J. Fyfe, V. Kattsov, A. Pitman, J. Shukla, J. Srinivasan, R. J. Stouffer, A. Sumi and K. E. Taylor (2007), Climate models and their evaluation, in *Climate Change 2007: The Physical Science Basis. Contribution of Working Group I to the Fourth Assessment Report of the Intergovernmental Panel on Climate Change*, edited by S. Solomon et al., Cambridge University Press, Cambridge, United Kingdom and New York, NY, US, pp 590–662.

Rayner, N. A., D. E. Parker, E. B. Horton, C. K. Folland, L. V. Alexander, D. P. Rowell, E. C. Kent, and A. Kaplan, (2003), Global analyses of sea surface temperature, sea ice, and night marine temperature since the late nineteenth century, *J. Geophys. Res.*, *108*(D14), doi:10.1029/2002JD002670.

Redi, M. H. (1982), Oceanic isopycnal mixing by coordinate rotation, *J. Phys. Oceanogr.*, *12*, 1154–1158.

Reick, C. H., T. Raddatz, V. Brovkin, and V. Gayler (2013), The representation of natural and anthropogenic land cover change in MPI-ESM, *J. Adv. Model. Earth Syst.*, doi:10.1002/jame.20022.

Roeckner, E., T. Mauritsen, M. Esch, and R. Brokopf (2012), Impact of melt ponds on Arctic sea ice in past and future climates by MPI-ESM, *J. Adv. Model. Earth Syst.*, *4*, MA00A02, doi:10.1029/2012MS000157.

Ross, C. K. (1984), Temperature-salinity characteristics of the "overflow" water in Denmark Strait during "Overflow 73", *Rapp. P-v Reun. Cons. Int. Explor. Mer.*, *185*, 111–119.

Schweiger, A., R. Lindsay, J. Zhang, M. Steele, H. Stern, and R. Kwok (2011), Uncertainty in modeled Arctic sea ice volume, *J. Geophys. Res.*, *116*, C00D06, doi:10.1029/2011JC007084.

Speich, S., B. Blanke, and W. Cai (2007), Atlantic meridional overturning circulation and the Southern Hemisphere supergyre, *Geophys. Res. Lett.*, *34*, L13612, doi:10.1029/2007GL031583.

Steele, M., R. Morley, and W. Emold (2001), PHC: A global ocean hydrography with a high-quality Arctic Ocean, *J. Clim.*, *14*, 2079–2087.

Stevens, B., et al. (2013), The atmospheric component of the MPI-M Earth system model: ECHAM6, *J. Adv. Model. Earth Syst.*, doi:10.1002/jame.20015, in press.

Sterl, A., R. Bintanja, L. Brodeau, E. Gleeson, T. Koenigk, T. Schmith, T. Semmler, C. Severijns, K. Wyser, and S. Yang (2011) A look into the ocean in the EC-Earth climate model, *Clim. Dyn.*, published online, doi:10.1007/s00382-011-1239-2.

Stouffer, R., et al. (2006), Investigating the causes of the response of the thermohaline circulation to past and future climate changes, *J. Clim.*, *19*, 1365–1387.

Sweby, P. K. (1984), High resolution schemes using flux limiters for hyperbolic conservation laws, *SIAM J. Numer. Anal.*, *21*(5), 995–1011.

Swingedouw, D., C. Rodehacke, E. Behrens, M. Menary, S. Olsen, Y. Gao, U. Mikolajewicz, J. Mignot., and A. Biastoch (2012) Decadal fingerprints of fresh water discharge around Greenland in a multimodels ensemble, *Clim. Dyn.*, in press.

Taylor, K. E., R. J. Stouffer, and G. A. Meehl (2012), An overview of CMIP5 and the experimental design, *Bull. Am. Meteorol. Soc.*, *93*, 485–498, doi:10.1175/BAMS-D-11–000941.

Talley, L. D., G. L. Pickard, W. J. Emery, and J. H. Swift (2011), *Descriptive Physical Oceanography: An Introduction*, 6th ed., 560 pp., Elsevier, Boston.

Talley, L. D., J. L. Reid, and P. E. Robbins (2003), Data-based meridional overturning streamfunctions for the global ocean, *J. Clim.*, *16*, 3213–3226.

Trenberth, K. E., and J. T. Fasullo (2008) An observational estimate of ocean energy divergence, *J. Phys. Oceanogr.*, *38*, 984–999.

Tsimplis, M. N., and H. L. Bryden (2000), Estimation of transports through the Strait of Gibraltar, *Deep Sea Res. I*, *47*(12), 2219–2242, doi:10.1016/S0967-0637(00)00024-8.

Valcke, S., A. Claubel, D. Declat, and L. Terray (2003), OASIS ocean atmosphere sea ice soil user's guide, *Tech. Rep. TR/CMGC/03/69*, 85 pp., CERFACS, Toulouse, France.

Voldoire, A., et al. (2012) The CNRM-CM5.1 global climate model: Description and basis evaluation, published online in *Clim Dyn.*, doi:10.1007/s00382-011-1259-y.

Wijffels, S. (2001), Ocean transport of freshwater, in *Ocean Circulation and Climate*, edited by G. Siedler et al., pp. 475–488, Academic.

Wolff, J. O., E. Maier-Reimer, and S. Legutke (1997), The Hamburg Ocean Primitive Equation Model HOPE, *Tech. Rep. 13*, 98 pp., German Climate Computer Center (DKRZ), Hamburg, Germany.

Woodgate, R. A., K. Aagaard, and T. J. Weingartner (2006), Interannual changes in the Bering Strait fluxes of volume, heat, and freshwater between 1991 and 2004, *Geophys. Res. Lett.*, *33*, L15609, doi:10.1029/2006GL02693.

Corresponding author: J. H. Jungclaus, Max Planck Institute for Meteorology, Bundesstrasse 53, D-20146 Hamburg, Germany (johann.jungclaus@zmaw.de)